CONVECTIVE HEAT TRANSFER PERFORMANCE OF SAND FOR THERMAL ENERGY STORAGE

A Thesis
Presented to
The Academic Faculty

by

Matthew Charles Golob

In Partial Fulfillment
of the Requirements for the Degree
Master of Science in the
School of Mechanical Engineering

Georgia Institute of Technology
August 2011

CONVECTIVE HEAT TRANSFER PERFORMANCE OF SAND FOR THERMAL ENERGY STORAGE

Approved by:

Dr. Sheldon M. Jeter, Advisor
School of Mechanical Engineering
Georgia Institute of Technology

Dr. Said I. Abdel-Khalik
School of Mechanical Engineering
Georgia Institute of Technology

Dr. Seyed M. Ghiaasiaan
School of Mechanical Engineering
Georgia Institute of Technology

Date Approved: 4/25/2011

To the students of Georgia Institute of Technology

ACKNOWLEDGEMENTS

I wish to thank my advisor Professor Sheldon Jeter for his guidance and insight on the project. I also want to thank Research Engineer Dennis Sadowski for his extensive assistance in setting up, running, and troubleshooting much of the experiments involved with this thesis. In addition, I want to thank graduate student Joel McKoy for his help on experimental analysis. I also want to thank undergraduates Duong T. Nguyen, Trevor Wolf, and Matthew Hoffman for their assistance in running the experiments. Finally, I want to thank my parents Charles and Elida Golob for supporting me and providing encouragement in this endeavor.

TABLE OF CONTENTS

LIST OF TABLES

LIST OF FIGURES

LIST OF SYMBOLS

K_p	Particle conductivity
K_g	Gas conductivity
K_f	Fluid conductivity
T_p	Plate temperature
h_s	Heat transfer coefficient of sand
$\dot{W}_{in}$	Electrical power input
A_c	Area contacted by sand
T_s	Sand Temperature
$\dot{Q}_a$	Heat leak rate due to air
A_{sur}	Heated area covered by sand
T_{sur}	Temperature of surface covered by sand flow
U_a	Random Uncertainty
U_b	Bias Uncertainty
U_c	Combined Uncertainty
d	Particle diameter
$\bar{h}$	Average heat transfer coefficient
χ	Empirical constant
β	Empirical constant
Pe_L^*	Péclet number
Fr^*	Froude number
U	Flow velocity
L	Length of heated plate

α	Thermal diffusivity of sand
k	Conductivity of sand
g	Gravitational acceleration
h	Thickness of sand layer
v	Solid fraction
v_c	Critical solid fraction (empirical constant)

LIST OF ABBREVIATIONS

TC	Thermocouple
TES	Thermal Energy Storage
HTF	Heat Transfer Fluid
CSP	Concentrator Solar Power
TPD	Thermal Particle Dynamics
DEM	Discrete Element Method
CFD	Computational Fluid Dynamics
EES	Engineering Equation Solver
PVC	Polyvinyl Chloride
DC	Direct Current
RTD	Resistive Thermal Device
SRTD	Standardized Resistive Thermal Device

SUMMARY

This thesis seeks to examine the effective convective heat exchange of sand as a heat exchange medium. The goal of this exploratory research is to quantify the heat transfer coefficient of sand in a proposed Thermal Energy Storage (TES) system which intends to complement solar thermal power generation. Standard concentrator solar thermal power plants typically employ a heat transfer fluid (HTF) that is heated in the collector field then routed to the power generators or TES unit. A fairly clear option for a TES system would be to utilize the existing HTF as the working storage medium. However, the use of conventional HTF systems may be too expensive. These fluids are quite costly as the quantity needed for storage is high and for some fluids their associated high vapor pressures require expensive highly reinforced containment vessels. The proposed storage system seeks to use sand as the storage medium; greatly reducing the expenses involved for both medium and storage costs. Most prior TES designs using sand or other solids employed them in a fixed bed for thermal exchange. The proposed TES system will instead move the sand to drive a counter flow thermal exchange. This counter flow design allows for a much closer temperature of approach when compared to a fixed bed. As cost and performance are the primary goals to tackle of the proposed system, the evaluation of the sand's thermal exchange effectiveness in a flowing state is necessary. Experiments will be conducted to measure the effective heat transfer coefficient between the sand and representative solid surfaces used as the heat transfer conduits. Additional experiments that will be looked at are wear caused by the sand as a consideration for long term design viability as well as angle of repose of the sand and its

effect on scoop design for improved materials handling. Key investigational aspects of these experiments involve the sand grain size as well as shape of the heat exchanger surfaces. The thesis will evaluate the resulting convective heat transfer coefficient of the sand as related to these features. The data will then be compared and verified with available literature of previously studied characteristic thermal properties of sand. The measured and confirmed data will then be used to further aid in a design model for the proposed TES system.

CHAPTER 1

INTRODUCTION

The following thesis covers the results of exploratory research on a proposed Thermal Energy Storage (TES) system which intends to complement solar thermal power generation. Specifically the focus of this paper is the evaluation of the heat transfer performance of sand as suitable thermal storage medium. Standard concentrator solar thermal power plants typically employ a heat transfer fluid (HTF) that is heated in the collector field then routed to the power generators or TES unit. A fairly clear option for a TES system would be to utilize the existing HTF as the working storage medium. Using conventional HTF's comes with some unfortunately stiff economic drawbacks. These fluids are quite costly as quantities needed for storage are high and their associated high vapor pressures require expensive highly reinforced storage facilities. The proposed storage system seeks to use sand as the storage medium; greatly reducing the expenses involved for both medium and storage costs. TES designs using sand or other solids in a fixed or non-kinetic medium state for thermal exchange suffer significant losses due to charge/discharge temperature drops. The proposed TES system will instead move the sand to drive a general counter flow thermal exchange. This counter flow design allows for a much closer temperature of approach as compared to a fixed bed. As cost and performance are the primary goals to tackle of the proposed system, the evaluation of the sand's thermal exchange effectiveness in a flowing state is necessary. Ongoing experiments are being conducted to measure the effective heat transfer coefficient between the sand and representative solid surfaces used as the heat transfer conduits.

Key investigational aspects of these experiments involve the sand grain size as well as shape of the thermal exchanger conduits.

Thermal Energy Storage Concept

Heat transfer to flowing particulates such as sand is not commonly encountered in thermal engineering applications. Nevertheless, one emerging interest is that sand could be used as the storage medium in a proposed thermal energy storage system. The proposed TES will be incorporated into an overall concentrator solar power (CSP) system. In operation, a conventional heat transfer fluid is heated in the collectors. This heat must then be transferred to and from sand acting as the storage medium. The overall TES design concept, illustrated in Figure 1.1 for the heat storage process, is to utilize a very inexpensive and benign storage medium, specifically ordinary silica sand or similar fine grained material. In operation, the sand is transported between separate insulated storage containers as the sand is heated and then the transport is reversed as stored heat is recovered from the sand. For a typical CSP trough system, the hot HTF from the solar field is around 370 C (700 F), and the fluid is typically returned at temperature around 270 C (520 F). In such an energy storage system, one container would contain only moderately warm sand close to 270 C that is available to be heated and store energy, and the other would contain the hot sand at around 370 C after it has been heated with HTF from the solar field to store energy.

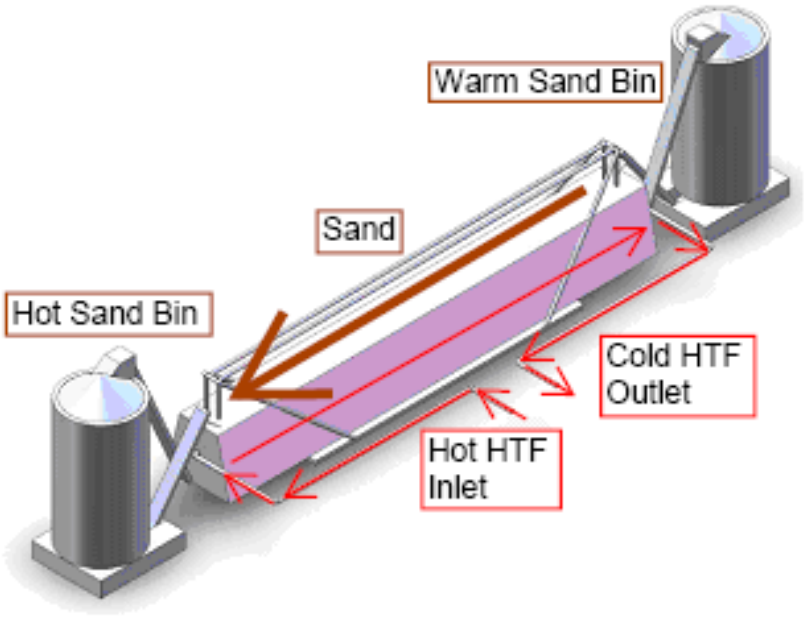

Figure 1.1 Conceptual Design of the Proposed TES System

Shows during heat storage with high and low temperature containers connected by Sand Shifter heat exchanger/conveyor.

The Sand Shifter

The HTF will both heat sand for storage during solar energy collection and recover heat from storage. Obviously, heat exchange is needed in any such indirect TES concept, in which different heat collection and storage media are used. The innovative enabling technology in this system is the combined sand conveyor and heat exchanger identified by our development team as the Sand Shifter.

The shifter moves the sand and HTF, in this case oil, in overall counterflow as heat is exchanged. The Sand Shifter itself is an innovative design that combines the functions of conveying sand and exchanging heat in one device. This system is currently

the subject of intellectual property applications, so its details will not be disclosed at present. Nevertheless, to understand the overall system and the engineering issues, it is only necessary to understand the general operation of the device. In the Sand Shifter, sand will be moved longitudinally between high and low temperature storage containers while the sand is simultaneously lifted and poured over finned tubes (or other metal conduits) that contain the counter-flowing HTF. The primary issue in this design is the performance of the heat exchange process between the flowing sand and metal surfaces. The achievable heat flux density largely dictates the overall sizing of the sand shifter and, as a result, its economic feasibility. The remainder of this thesis addresses some preliminary measurements of the coefficient of heat transfer between flowing sand and a heat exchange surface.

CHAPTER 2

LITERATURE REVIEW

When looking at current literature on particle interaction there are several subsets of interest: fluidized bed heat transfer, heat transfer in an immobile bed of particles, particle flow, and heat transfer in a moving bed of particles. Because convection from the gas to the particle plays a much higher role in a fluidized bed it would be expected that these would have little relevance to the current project, however, there are a number of papers modeling the heat transfer between particle-particle and particle-surface interactions [1-3]. These mostly use a kinetic/collision theory approach to determine the heat transfer. The papers on immobile beds focus on the effective conductivity of the particles using thermal particle dynamics (TPD) [4-6]. The particle flow papers can be broken up into two different types, kinetic theory based flow for low particle density (falling particles/fluidized beds) [7] and shear based flow for denser particle flow [8-9]. The heat transfer in a moving bed of particles can be further broken up into heat transfer in a rotary vessel using discrete element method (DEM) modeling [6,10-11] which are numerical methods for computing the motion of a large number of individual particles on the micrometre-scale and above. The remaining set are direct experiment based heat transfer models for a moving bed of particles [12-18].

Particle Interaction

Süle et. al. [1] used a population balance model which takes into account the particle-particle and particle-wall collisions to describe heat transfer processes in fluid-solid systems and employs a compartment model to describe the spatial distribution of

the temperature in a back-flow model. Both the particle-particle and particle-wall heat transfer are modeled by collisions with random parameters. The results of this showed that the intensity of inter-particle collisions play a significant role in reducing the temperature dispersion of particles, while increasing fluid-particle heat acts inversely. In Sun et. al.'s [2] investigation, the particle impact heat conduction through time varying contact area during impact was examined for the purpose of quantizing the direct conductive contribution of heat transfer between particles and surfaces in suspension flow and fluidized beds. Sun et. al. found that this heat transfer mechanism does not appear to be dominant in fluidized bed under typical conditions. Natale et. al. [3] report experimental results on the heat transfer between a fluidized bed of fine particles and a submerged surface. Their results show that the heat transfer coefficient increases with particle Archimedes number and is almost independent from particle thermal conductivity for $K_p/K_g>30$.

Thermal Particle Dynamics

Vargas, et. al. [4] investigated the heat conduction in a packed bed of cylinders both experimentally and computationally using the discrete element method. By explicitly modeling individual particles within the bulk material, bed heterogeneities are directly included and dynamic temperature distributions are obtained at the particle level. They found that stress chains in a particle bed tended to augment heat flow along a particular axis while hampering heat transfer perpendicular to that axis. Vargas, et. al. [5] also extended the numerical technique and the thermal particle dynamics method to study heat conduction in granular media in the presence of stagnant interstitial fluids. Vargas, et. al. determined when $K_p/K_f>>1$, TPD provides good qualitative and quantitative agreement between measured and calculated values of the effective conductivity for a wide variety of materials and for packed beds at different loads in the presence of both

liquid and/or gases. Furthermore, Vargas-Escobar's [6] thesis addresses heat conduction in granular systems both under static and slow flow conditions with and without the presence of a stagnant interstitial fluid using the TPD method. For a rotating drum flow, Vargas distinguished the mechanisms by which the heat transport process takes place: at low shear rates (small mixing factor), conduction through particle contacts dominates due to lasting contacts; as the shear rate increases (larger mixing factor), convective mixing caused by an increased granular temperature enhances the transport of heat and therefore the effective conductivity increases proportionally. The latter analysis also included DEM modeling.

Particle Flow

Lun, et. al. [7] studied the flow of granular material using statistical methods analogous to those used in the kinetic theory of gases. Two theories were developed: one for the Couette flow of particles having arbitrary coefficients of restitution (inelastic particles) and a second for the general flow of particles with coefficients of restitution near 1 (slightly inelastic particles). Approaching from a different angle using a dense particle arrangement, Thompson, et. al. [8] described molecular-dynamics simulations of non-cohesive granular assemblies under shear. Low shear rates exhibit stick-slip dynamics, while steady-state motion occurs at larger shear rates with a static and a flowing layer. Also for dense particle flow, Baxter, et. al. [9] described dynamic measurements of the stress obtained during a sand flow. The data showed a large noise component.

Discrete Element Method Modeling

Shi, et. al. [10] employed a computational technique that couples the DEM, computational fluid dynamics (CFD), and heat transfer calculations to simulate realistic heat transfer in a rotary kiln. They found that at low particle conductivities, the heat transfer is dominated by gas–solid conduction; however, at higher particle conductivities solid–solid conduction plays a more important role. This is similar to the results found in Vargas's work. Chaudhuri, et. al. [11] used the discrete element model to simulate the dynamic behavior of cohesive and non-cohesive powder in a rotating drum (calciner) and double cone (impregnator). The granular material was considered as a collection of frictional inelastic spherical particles. Each particle was able to interact with its neighbors or with the boundary only at contact points through normal and tangential forces. The model simulated flow, mixing, and heat transport in granular flow systems for the rotary calciners and impregnators. Their simulations showed that as rotation speed decreases, both heat transfer and temperature uniformity of the granular bed for both calciner and impregnator increase.

Heat Transfer in Moving Bed of Particles

Molerus [12] reported that the contact resistance for the heat transfer between adjacent particles was the limiting factor for heat transfer in moving beds of particles consisting of rather hard solid materials and filled with a stagnant interstitial gas. Brinn, et. al. [13] measured slug flow of sand flowing through a pipe. They found better heat transfer coefficients in smaller inner diameter pipes with increased flow rate, further improving the heat transfer. The heat transfer coefficient for slug flow in the pipe cases were found to range between 40~120 W/m^2-K. The overall purpose of the experiments

was to create a theoretical model of the heat transfer mechanics of the pipe flow. Measurements done by Denloye, et. al. [14] noted that the flowing packed bed to surface heat transfer coefficient increases with decreasing residence time, decreasing particle size, and increasing gas thermal conductivity. Regarding the residence time, they indicated the increase in heat transfer coefficient was more pronounced for smaller particles. In the experiments using air/sand, Denloye, et. al. (1977) measured maximum heat transfer coefficients of ~125 W/m^2-K for 2370 μm sand, ~310 W/m^2-K for 590 μm sand, and ~475 W/m^2-K for 160 μm sand. Hyde, et. al. [15] measured a range of materials heat transfer coefficients using a fluidized bed. Bubbling air through sand they measured ~300 W/m^2-K for 560 μm sand, ~360 W/m^2-K for 450 μm sand, ~405 W/m^2-K for 295 μm sand, and ~450 W/m^2-K for 225 μm sand. Determination of heat transfer between the fluidized bed and the heating or cooling elements submerged in the bed was carried out by calculating the maximum heat transfer between a sphere and a wall under brief contact, as well as taking into account the addition of the void fraction of the stationary packing and bed expansion. Patton, et. al. [16] proposed a model relating the Nusselt number to a Péclet number and a Froude number. The predicted results of the model were compared with the experimental data from heat transfer over a flat plate. The experimental model was able to estimate a heat transfer coefficient for the flowing sand over a surface using a well-defined set of parameters. Another report by Babcock and Wilcox in 1981 [17] looked into a range of TES options including sand. They predicted based on Denloye, et. al.'s (1977) work that with a moving bed of fine grained sand they would achieve a heat transfer coefficient on their charging heat transfer elements for steam to the sand of ~930-1160 W/m^2-K and a coefficient of ~803-1308 W/m^2-K on the

discharge side. Green, et. al. [18] did further exploration into thermal energy exchange systems and using a shell and tube design reported an expected heat transfer coefficient of ~1470 W/m^2-K for the sand side in that configuration. This result, though, was based in part from the flowing sand predictions in the Babcock and Wilcox (1981) report. The range of heat transfer coefficients from the various pieces of literature have been tabulated below in Table 2.1.

Table 2.1 Heat Transfer Coefficients for Moving Sand Reported in Literature

Authors	**Description**	**Heat Transfer Coefficients**
Brinn, et. al. (1948)	Slug flow of sand in pipes.	40~120 W/m^2-K
Denloye, et. al. (1977)	Packed bed flow over heated surface.	125 W/m^2-K~475 W/m^2-K Sand: 2370 µm-160 µm
Hyde, et. al. (1980)	Heat transfer for air/sand fluidized bed.	300 W/m^2-K~450 W/m^2-K Sand: 560 µm-225 µm
Patton, et. al. (1986)	Heat transfer model for flowing granular material.	Olivine: 550~890 W/m^2-K Silica: 290~650 W/m^2-K
Babcock and Wilcox (1981)	Steam to flowing bed of sand heat exchanger.	Charge: 930~1160 W/m^2-K Discharge: 800~1310 W/m^2-K
Green, et. al. (1986)	Shell and tube heat exchanger using air and sand	~1470 W/m^2-K

Heat Transfer Model

Examination of the literature reveals a few important details, the computational particle interaction or DEM models while useful in understanding the heat transfer mechanics were limited and unwieldy for comparative purposes. Furthermore there is a large range of empirical results for moving beds of particles, each with their own set of contingent conditions. It is therefore prudent to experimentally verify the heat transfer coefficient for the intended conditions. Of the literature on particulate flow, Patton et. al.'s [16] results based on flow over a plate were the best match for a comparative model analysis with the Sand Shifter's flow concept. Patton's model is noted in Appendix A. The convective heat transfer coefficient of flowing sand was modeled in Engineering Equation Solver (EES) [19] based on the relations found in Patton, J. S., et. al.(1986) [16] to compare it to the convective heat transfer coefficient determined experimentally. The heat transfer coefficient was determined for two types of sand. Olivine sand was experimentally measured (Appendix B) to have a mean diameter of 78 μm with a standard deviation 30 μm. Silica sand was measured to have a mean diameter of 0.55 mm with a standard deviation of 0.32 mm. The conductivity, heat capacity, and density were obtained from the EES materials property package and the properties were assumed to be similar for both olivine and silica with olivine slightly denser. The velocity of the sand layer was estimated to be between 0.15~0.3 m/s, the thickness of the layer to be 0.4 mm to 2 mm, and the packing ratio between 0.2 and 0.42. Using these parameters, the convective heat transfer coefficient was estimated to be between 550~890 W/m^2-K for the olivine and 290~650 W/m^2-K for the silica. The flat surface experimental results, found in this paper, of ~550-900 W/m^2-K for olivine and ~200-400 W/m^2-K for Silica

fall within or near the models predicted range. These values also were near those found in Denloye, et. al.'s [14] packed bed of flowing sand measurements and Hyde, et. al.'s [15] fluidized bed measurements. Of the factors that affect the heat transfer, particle size had the dominant effect on the heat transfer coefficient, followed by velocity, and finally the layer thickness and packing ratio. On the higher range of reported results, Babcock and Wilcox in 1981 [17] indicated an expected heat transfer coefficient, on their charging heat transfer elements, of ~930-1160 W/m^2-K using a moving bed of sand. The sand utilized in Babcock and Wilcox report had a grain size of 44-77 μm, a packing ratio of 0.40, and a sand velocity ~0.15-0.3 m/s, which is right around the range of the olivine sand of the current experiment. Their results and those of Green, et. at. [18] suggest possibility for higher effective thermal transfer through the shape of the transfer surface. Furthermore Muchowski [20] and Wunschmann, et. al. [21] reported that vibrating the vessel could yield a small improvement in the heat transfer coefficient for a particulate such as sand. These studies indicated that small vibrations had a positive effect on the heat transfer coefficients (an enhancing effect was observed) but the trend did not continue at large vibrational accelerations. Another important side effect of vibration is that it allowed sand to flow on much shallower slopes, allowing the angle of repose limit for natural gravity driven flow, covered in Chapter 5, to be circumvented.

CHAPTER 3

FLAT PLATE HEAT TRANSFER EXPERIMENT

Since heat transfer to flowing sand is not a familiar process, a preliminary, almost expedient, scoping experiment was conducted. This preliminary investigation of the heat transfer coefficient, defined in Equation (1), was conducted for two candidate materials, olivine and silica sands. Olivine was chosen for its established good performance in some foundry sands. As quantified by Equation (1), the overall experimental concept was to determine the heat transfer coefficient from measurements of the temperature of the free stream flowing sand and the temperature of the heat transfer surface, which is heated with a known power input.

Flat Plate Setup

The preliminary setup used an inclined flat surface. The heat source was a flat plate electric heater 152 mm x 152 mm square mounted beneath an aluminum heat transfer plate. Both flat plates and plates with square fins machined into the surface were studied. The fins were 3.18 mm (1/8 inch) high by 3.18 mm wide with 3.18 mm spacing. As shown in Figure 3.1, the aluminum heat exchange plates were placed on the heater plate. This assembly was inset into insulating board to prevent heat leaks, leaving only the upper surface of the aluminum plate exposed. A 3 x 3 evenly spaced grid of T-type thermocouples were then placed in small diameter shallow holes which were drilled into the aluminum plate and secured in place with a small amount of thermal cement. The surface temperature measurements were averaged to characterize the plate temperature (T_p). A large storage bin for sand with a dispenser nozzle at the bottom was placed above

the plate. Gravity, assisted by vibration, allowed the sand to easily flow from the bin over the heated surface. A thermocouple placed in the flowing sand just upstream of the dispenser measured the free stream temperature of the sand. With the hot plate operating at a known electrical power input, measurements of the temperature of the plate surface and the incoming sand were taken, while a visual estimate of the contacted area (i.e. the portion of exposed surface covered by sand) of the flow over the plate was made. The "contacted" area of the flat plate was taken to be between 95-99% with only the top corners left uncovered. For the finned plate, the contacted area was seen to exclude the bottom third of the tops of the finned surface due to insufficient sand submersion. Intentionally this was a conservative estimate that should not exaggerate the heat transfer coefficient. The heat transfer coefficient was then calculated as follows:

$$h_s = \frac{\dot{W}_{in}}{A_c \cdot (T_p - T_s)} \tag{1}$$

Here the heat transfer coefficient of sand is represented by h_s, $\dot{W}_{in}$ is the electrical power (W) input, A_c is the area (m²) contacted by the sand, T_p is the plate temperature (K) measured by the embedded thermocouples, and T_s is the free stream sand temperature (K) measured by the upstream thermocouple.

Flat Plate Measurements

This apparatus and method was applied to both silica and olivine sands and repeated for both flat and simple square finned plate designs.

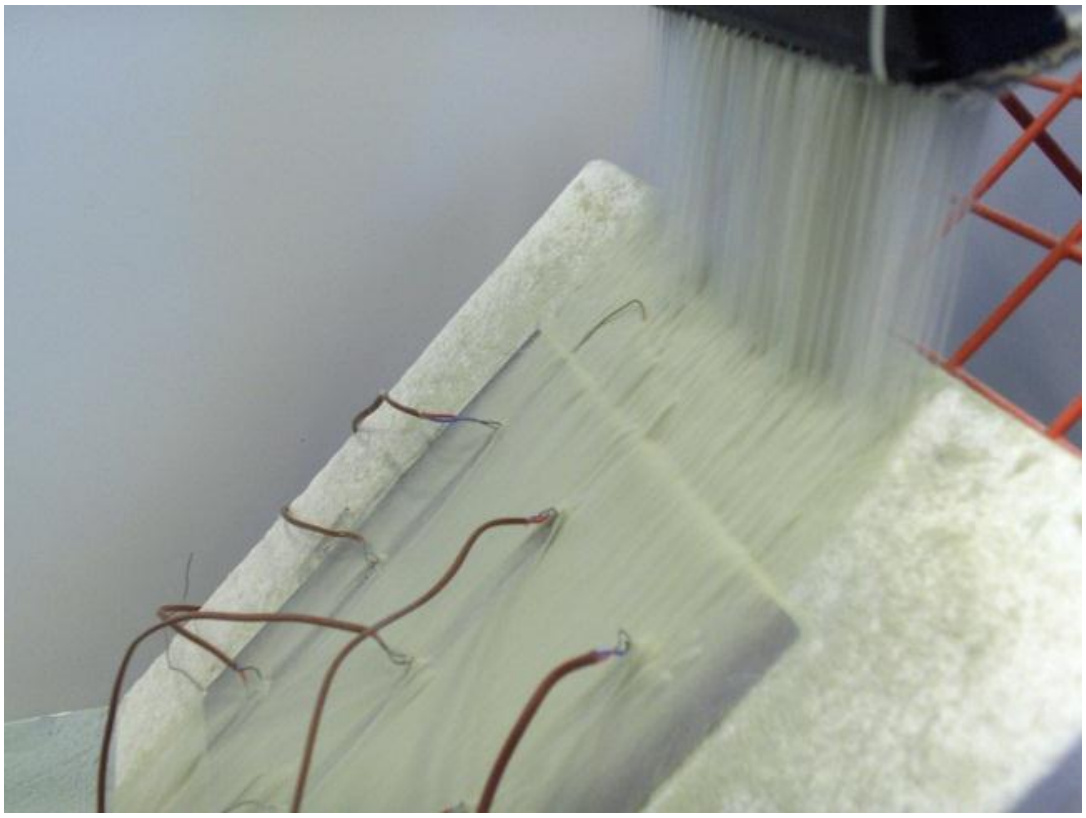

Figure 3.1 Preliminary Heat Exchange Experiment for Flow over Heated Flat Plate
Sand is flowing from nozzle over the plate.

Figure 3.1 shows sand flowing over a heated instrumented plate in one of our earliest experiments. As seen in the photo, the sand from the hopper is dispensed over the heated plate. Measurements of the plate surface and sand free stream temperatures were taken when the system reached a steady state, *i.e.* approximately constant temperature difference.

More than 30 experiments of various combinations and configurations were run. The convection coefficient varied with plate temperature and contacted area, so it was difficult to assign a specific value to each type of sand. However, olivine sand appears to have a higher convection coefficient than silica sand. The ranges of measured heat transfer coefficients are given in Table 3.1.

Table 3.1 Heat Transfer Coefficients for Sand Types and Configurations

Configuration	Sand Type	Heat Transfer Coefficient (W/m^2-K)
Flat	Silica	310-400
Finned	Silica	212-405
Flat	Olivine	550-925
Finned	Olivine	375-635

It was somewhat surprising to see that sand flowing over a flat plate shows a higher convection coefficient than that flowing over a finned plate, even after a correction for the contact area. It appears this shortcoming was a failure of the sand to continuously submerge all the fin surfaces as shown in Figure 3.2.

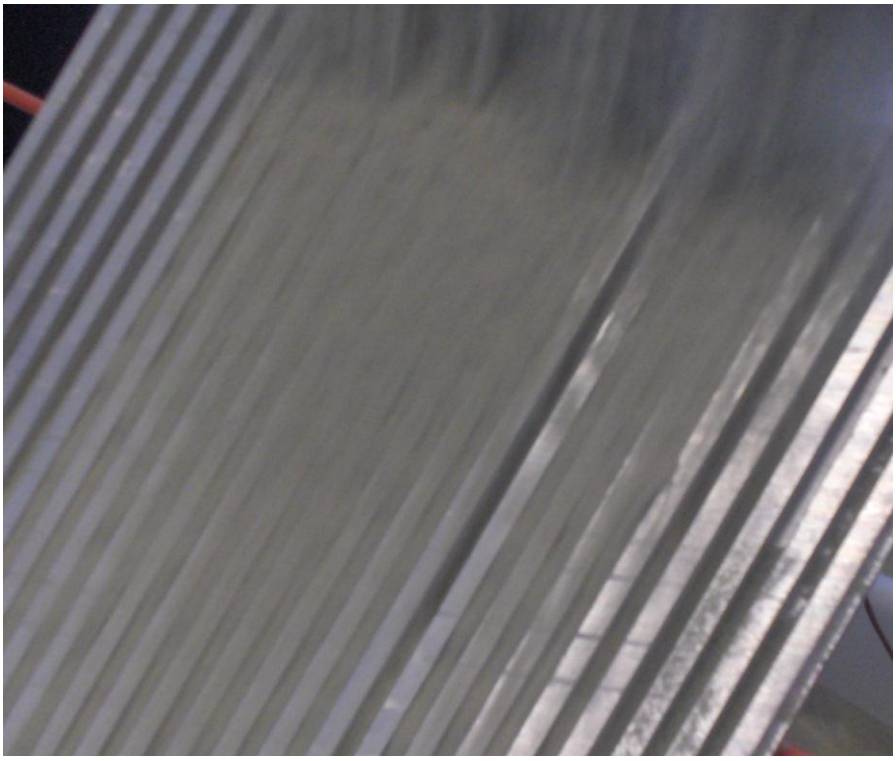

Figure 3.2 Sand Flow on Square Finned Surface

Note the sand rarely has contact with the tips of the fins.

While this apparatus was helpful for screening experiments, it had several severe shortcomings: (1) The test articles were effectively limited to simple flat plates which were not representative of the finned tubes that might be used in practice. (2) The test could only be run continuously with great effort because the reservoir had to be refilled manually. (3) The test could not be run for long periods over a range of temperatures. These shortcomings were resolved by the development of the continuous drum device described in chapter 6.

CHAPTER 4

SAND EROSION TRIALS

The purpose of the sand erosion trials was to examine the wear effect of different types of sand on the primary interface portion of the heat exchange tubing. The experiment evaluated the wear of the sand on the heat exchange tubing through mass loss. This was done through employing a rotating tumbler with internal scoops angled to pour the sand over the tubing thus subjecting it to continuous exposure. Through periodic measurements of the tube and fin assembly mass, a loss rate associated to the sand wear on the heat exchange tubing could be estimated.

Setup and Methodology

The major equipment for the sand exposure experiment included a re-sealable plastic container, a 12V DC motor to rotate the container, and an aluminum base plate to mate the container to the motor's drive shaft. The container was a 4.4 liter re-sealable plastic bowl. To direct sand flow in the container as it was rotated pouring sand over the test piece, fins made of aluminum edging were cut. These fins were then attached to the inside of the container using rivets. When rotated, this ensured continuous sand flow over the heat exchange tubing. For the drive to the rotate the container, a 12V DC motor was employed and mounted to a secure support. The motor ran at 12-15 rpm to maintain constant sand flow over the finned tube in the container. The setup had the sand falling on the test article as being between ~0.5-0.7 m/s according to gravity calculations. Joining the container to the drive shaft was a rigid coupling secured by lead screws. The end of the coupling was welded to a circular aluminum base plate. The base plate had

three equidistance screw holes through which the plastic container was secured to the base. The test piece was next weighed with a precision of +/-0.001g to determine the base mass. To mount the test piece, a hole was drilled in the center of the container lid to a diameter just less than the diameter of the heat exchange tubing. The tube end was then forced through the hole ensuring a very snug seal as well as holding the test piece rigid. Sand was then added to the container and the lid reapplied and sealed. The motor was then activated, with the rotation of the internal aluminum fins to ensure continual sand flow over the test piece. Periodically the assembly would be stopped and the test piece removed for weighing to the nearest 1 mg. The test piece would then be returned to the container and the device run again. The following Figure 4.1 shows a view of the erosion assembly with the lid removed.

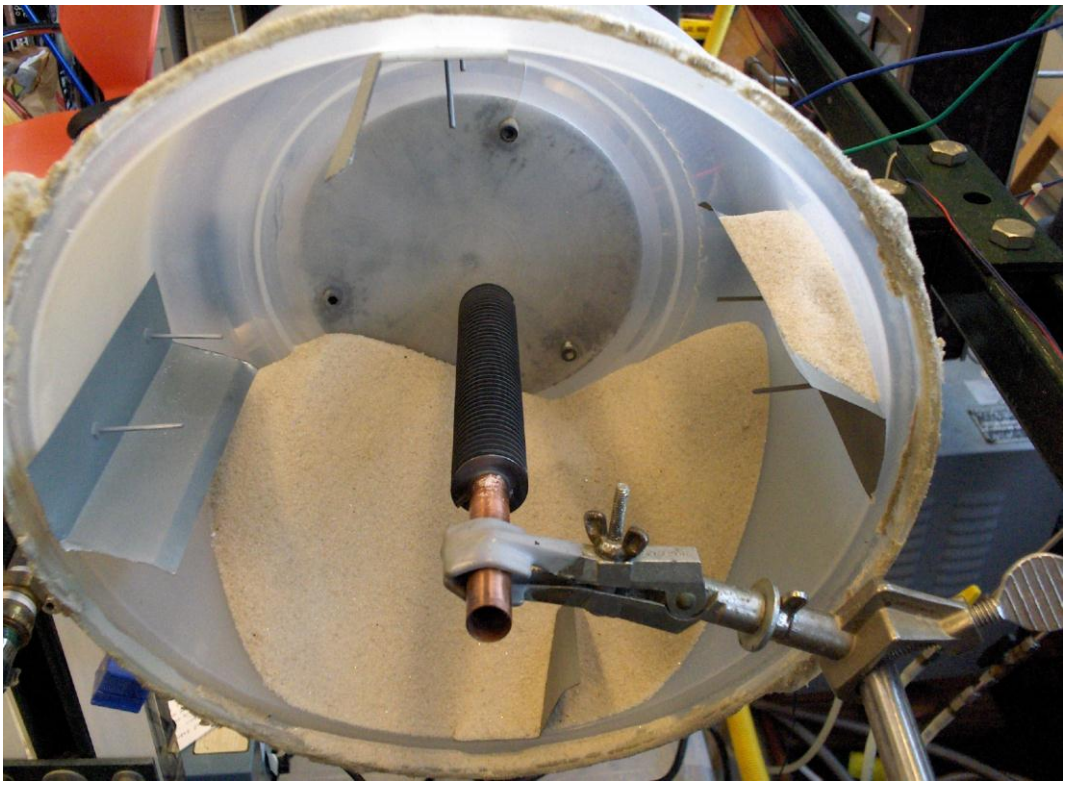

Figure 4.1 Sand Erosion Assembly

Wear Measurements

The following tables contain the mass measurement data for the aluminum fin trial and the ongoing data for the steel fin trial. From this table, a wear rate by sand type can be estimated. The measured results of the aluminum fin trial can be found in Table 4.1.

Table 4.1 Aluminum Finned Copper Tube Trial Data, Silica Sand

Silica Sand Erosion Trial			Continuous sand exposure	
	Short Aluminum Finned Copper Tube		0.0417	% mass loss a day
Date	(Days)	Scale 1 +/- 0.001g mass(g)	Rate(g/day)	Scale 2 +/- 0.1g mass(g)
3/18/2009	0	102.365		102.9
3/19/2009	1	102.249	0.11600	102.8
3/27/2009	9	101.860	0.05611	102.4
3/31/2009	13	101.810	0.04269	102.3

Even with a conservative rate of 0.04% loss per day. The subject tubing would lose 1% of its total mass after less than a month of continuous exposure. Visual inspection also revealed a significant degree of apparent wear. As a result a more durable steel finned copper tube would be tested.

Table 4.2 Steel Finned Copper Tube Trial Data, Silica Sand

Silica Sand Erosion Trial			Continuous sand exposure	
		Short Steel Finned Copper Tube Scale 1 +/- 0.001g	0.0037	% mass loss a day Scale 2 +/- 0.1g
Date	(Days)	mass(g)	Rate(g/day)	mass(g)
5/8/2009	0	70.027		70.4
5/12/2009	4	69.993	0.00850	70.4
5/22/2009	14	69.984	0.00307	70.4
6/4/2009	27	69.951	0.00281	70.3
6/16/2009	39	69.939	0.00226	70.3
6/22/2009	45	69.926	0.00224	70.3
6/29/2009	52	69.922	0.00202	70.3
7/9/2009	62	69.894	0.00215	70.3
7/29/2009	82	69.813	0.00261	70.3

The copper tube steel finned had a far lower loss rate as seen in Table 4.2. At 0.0037% mass loss a day it would take about 9 months of continuous exposure to lose 1% of its total mass. In addition, the steel plating displayed significantly less visual wear than the aluminum.

Due to its promising convection values, further examination of the olivine sand characteristics was needed. One of the key factors to investigate was what kind of wear rate would the olivine have compared to the silica on the steel fins. To do this the same format and assembly of a tumbler was made for the olivine erosion trial.

Table 4.3 Steel Finned Copper Tube Trial Data, Olivine Sand

Olivine Sand Erosion Trial			Continuous sand exposure	
	Short Steel Finned Copper Tube		-0.0012	% mass loss a day
Date	(Days)	Scale 1 +/- 0.001g mass(g)	Rate(g/day)	Scale 2 +/- 0.1g mass(g)
6/16/2009	0	59.413		59.8
6/22/2009	6	59.548	-0.02250	59.8
		(could not get all the sand dust off)		
6/29/2009	13	59.414	-0.00008	59.8
7/9/2009	23	59.430	-0.00074	59.8
7/29/2009	43	59.449	-0.00084	59.8

The results in Table 4.3 for the next olivine trial indicated a small increase in measured weight. This was likely due to a difficulty of fully cleaning the fine olivine sand particles off the test piece. Even with extensive cleaning, the part with a high pressure air hose the mass measurement indicated a small gain. It should be noted though that this piece demonstrated no visual erosionwear even after 43 days of continuous running.

Further erosion tests using both olivine and silica sand were conducted on steel tube and fin assemblies. These were done in the same fashion as earlier trials, with initial masses taken and the tubes subjected to the constant pouring of sand in the tumbler. The masses were recorded periodically for determining a wear rate.

Table 4.4 Steel Finned Steel Tube Trial Data, Silica Sand

Silica Sand Erosion Trial			Continuous sand exposure	
	Steel Finned Steel Tube		0.0004	% mass loss a day
Date	(Days)	Scale 1 +/- 0.001g mass(g)	Rate(g/day)	
9/23/2009	0	152.005		
10/5/2009	12	151.992	0.00108	
10/6/2009	13	151.985	0.00154	
10/16/2009	23	151.981	0.00104	
11/5/2009	43	151.978	0.00063	

With silica sand, the steel tube steel fin wear rate at 0.0004% mass a day was an order of magnitude less than the copper tube steel fin assembly. It would take about 7 years of continuous exposure for it to lose 1% of its total mass. Inspection of the piece showed no appreciable wear.

Table 4.5 Steel Finned Steel Tube Trial Data, Olivine Sand

Olivine Sand Erosion Trial			Continuous sand exposure	
	Steel Finned Steel Tube		-0.0005	% mass loss a day
		Scale 1 +/- 0.001g	0.0000	% mass loss a day
Date	(Days)	mass(g)	Rate(g/day)	
9/23/2009	0	149.871		Start
10/6/2009	13	149.888	-0.00131	
10/9/2009	16	149.883	-0.00075	End
		(Piece slipped loose of mount and tumbled)		
10/12/2009	0	149.806		Start
10/16/2009	4	149.803	0.00075	
11/5/2009	20	149.806	0.00000	End

Like with copper tube steel fin assembly there was little change in the test object mass. Despite air cleaning the mass of the assembly changed little, even increasing. No apparent visual wear was present but the loss rate was decidedly small.

As experimentation on the project regarding the heat transfer coefficient progressed, it became more apparent that the small grain sand would be preferred, which also coincided with the erosion results. Improvements were also made to the sand erosion apparatus. A more secure mount for the test samples was added to prevent the test pieces from breaking off and tumbling and a rotating seal was inserted to further limit sand leakage. Figure 4.2 shows the modifications.

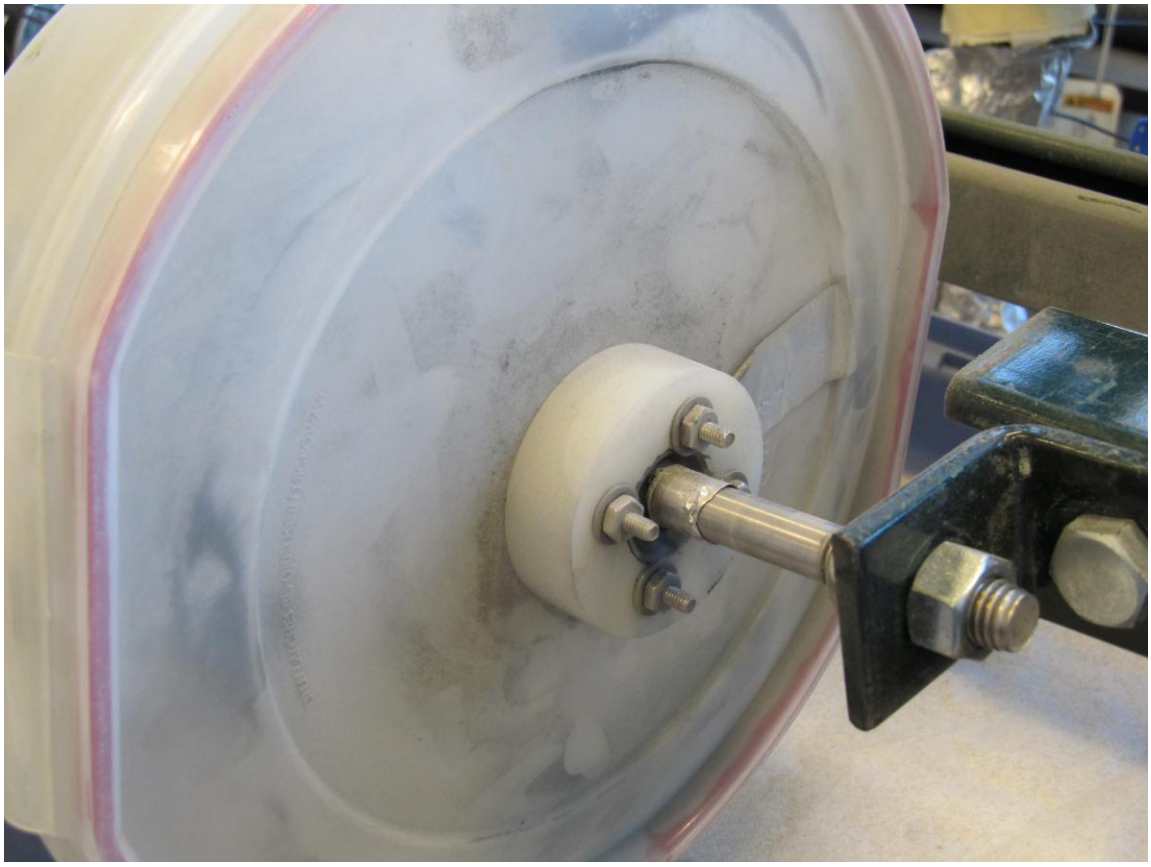

Figure 4.2 Improved Sand Erosion Apparatus

For final design purposes, steel was likely the material of choice both for its structural strength and viability at the target operating temperatures. With the prior test samples, steel had proved to be the least susceptible to sand erosion. Taking this in to account, an erosion trial was set up using CR-12, or Cromgard [22] steel. This steel was judged to have potential as it was considered to be more resistant to abrasive effects than regular steel, and it still maintained good structural strength at higher operating temperatures. The results of the trial are shown below in Table 4.6.

Table 4.6 Cromgard Sample Data, Olivine Sand

Olivine Sand Exposure Trial			Continuous sand exposure	
	Cromgard Sample Piece		-0.0001	% mass loss a day
Date	(Days)	Scale 1 +/- 0.001g mass(g)	Rate(g/day)	
12/15/2010	0	152.290		
1/3/2011	19	152.305	-0.00079	
3/21/2011	96	152.309	-0.00020	

Similar to the steel fin assembly, there was little change in the Cromgard sample mass. In fact there was measured a slight increase in mass, despite the thorough air cleaning. After nearly 100 days of constant exposure, inspection showed some slight surface build up as indicated in Figure 4.3. The lighter color zone was protected from the falling sand, while there was a slight dark discoloration in the remaining exposed surfaces. The edges experienced a slight buildup of dark discoloration as well.

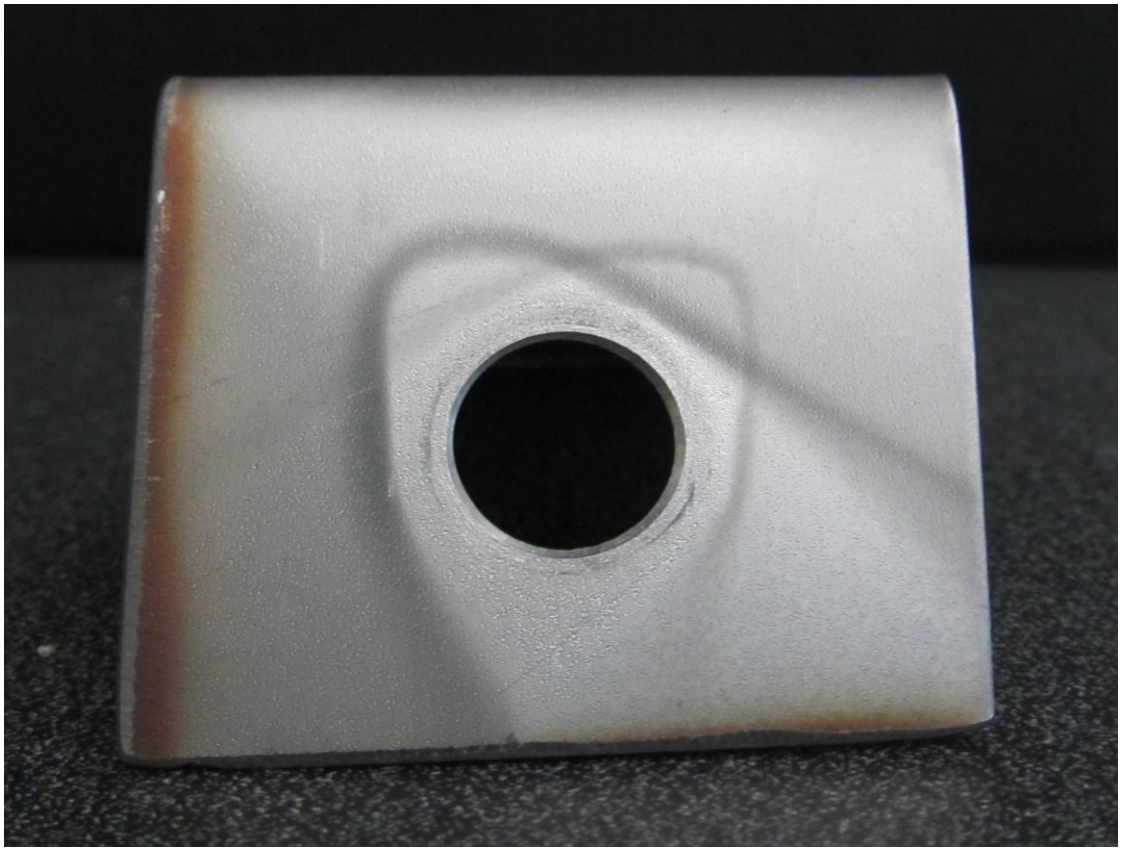

Figure 4.3 Cromgard Inspection

Sand Erosion from Grinding

Figures 4.4 and 4.5 below are of the half-inch diameter steel shaft from the sand erosion experiment. Figure 4.4 shows the eroded shaft next to a new shaft. Figure 4.5 is a close-up of the eroded section. The erosion is due to sand trapped between the shaft and a pair of rubber u-cup seals. The relative rotational speed between the shaft and the seals was ~12 RPM and was continuous for approximately 15 weeks. The shaft has been replaced by another one having a much closer fit between the shaft OD and seal ID and has been running continuously since March 18th. This case does demonstrate that trapped sand can be quite erosive when in a position to be ground into a surface.

Figure 4.4 Comparison between Shaft Grind Wear, new and old

Figure 4.5 Close up for Sand in Shaft Grind Wear

Erosion Conclusion

The aluminum exposure trial indicated a fairly high erosive rate when exposed to silica sand. Steel proved to be far more resistant to the silica wear on an order of magnitude of more than 10 times compared to both the aluminum finning and copper tubing cases. This was confirmed visually by surface inspection. It should be noted that when testing alumina beads, the beads proved to be destructive immediately, incurring visually apparent damage not only to the finned tubes but also to the scoops used in the apparatus. This damaging aspect was also noted in the heat transfer measurements were the flow speed was slower than the erosion trials, Appendix D, further use of the alumina was halted after heat transfer measurements showed it preformed significantly less than modeled predictions. Investigation of olivine sand on the steel finned tubing and particularly with the Cromgard sample yielded interesting results. The olivine sand, although accumulating in hard to clean portions of the finned tube assembly, did not appear to be incurring any noticeable visual wear. Similarly even after extensive exposure to the sand there was noted to be no visible wear for the Cromgard sample and even some dark color build up was detected. The empirical mass measurements indicate minimal wear at best, with no a discernable wear rate that yet can be ascertained. Overall it seems the smaller particles at these low speeds ~0.5-0.7 m/s, due to gravity and higher than in application, Appendix D, do not appear to have enough kinetic energy to impart meaningful deformation and wear when striking the surfaces. In addition, the smaller particles tended to behave much more like liquids and tended to flow more smoothly over a surface rather than somewhat raking surfaces as found with the larger solid particles.

CHAPTER 5

SAND SCOOP DESIGN

Sand Angle of Repose

When sand or other granular material is poured into a pile from above, it can form a marginally stable conical pile. The angle between the sloped side and the horizontal is the angle of repose. The angle of repose is a function of the grain size and the interaction of friction between grains. It is helpful to know the angle of repose when designing the scoops which lift the sand from the bottom of the drum and rain it upon the heat exchanger tube bundle. This angle is important as the sand will not naturally flow by gravity alone when on slopes less then this angle, and from knowing this angle one can determine the pouring point for a scoop. It is also needed in other analytical models and in modeling how fully the sand will occupy the pits or silos.

In the improved experiments, the equipment consisted of a transparent acrylic plastic disc, a support brick, and a PVC pipe. The acrylic disc was placed on the top face of the brick in a position where there was no overhang on one side. The PVC pipe was then placed flush against the free surface of the Plexiglas plate, as shown in Figure 5.1.

Figure 5.1 Angle of Repose Test Setup

Sand was poured into the PVC pipe until it was approximately full. The PVC pipe was lifted vertically while trying to have minimal horizontal displacement relative to the acrylic disc. Lifting speed of the PVC pipe did not matter so long as it was lifted in a reasonably fast manner. Upon completion of the sand flow, a cone shaped mound of sand would remain on the surface of the acrylic plate shown in Figure 5.2.

Figure 5.2 Angle of Repose

Using the side without any overhang from the acrylic disc for vertical registration, a square was used to measure the height of the mound of sand. Based on the premise that the mound of sand could be modeled by a cone, the arctangent of the height and half the diameter of the acrylic disc was used to calculate the angle of repose of the sand. For the silica sand the measured angle of repose was about 30 degrees, which was expected, and for the finer and denser Olivine it was about 42 degrees. This angle played a small but

important role in the scoop design, in determining each scoop load size, and duration of pouring.

Sand Scoop Optimization

The task of moving material through the sand shifter was two-fold. First, hot sand had to be conveyed along the axis of the heat exchanger with the use of an Archimedes screw. Second, sand had to be lifted in the circumferential direction so that a steady flow of hot material can be poured over the heat exchanger articles. This was accomplished with the use of longitudinal scoops which were positioned in segments between the Archimedes screw threads. The volume of sand carried by each scoop primarily depended on the scoop profile, the type of sand being used, and the angle of repose that was established by the sand as it piled at the top of a filled scoop. Another important factor to consider was how evenly the sand was poured across the heat exchanger tubes. A design that maintained a more even distribution of sand flow across the tube bundle would be superior to a scoop that deposited 50% of its contents on just 20% of the articles.

To measure this, a test device was constructed for the purpose of optimizing the sand distribution over the heat exchanger articles. Shown in Figure 5.3, the device consisted of a frame, a drum that was rotated via a drive belt, and an array of trays that was supported in the axial center of the drum with cantilever beams.

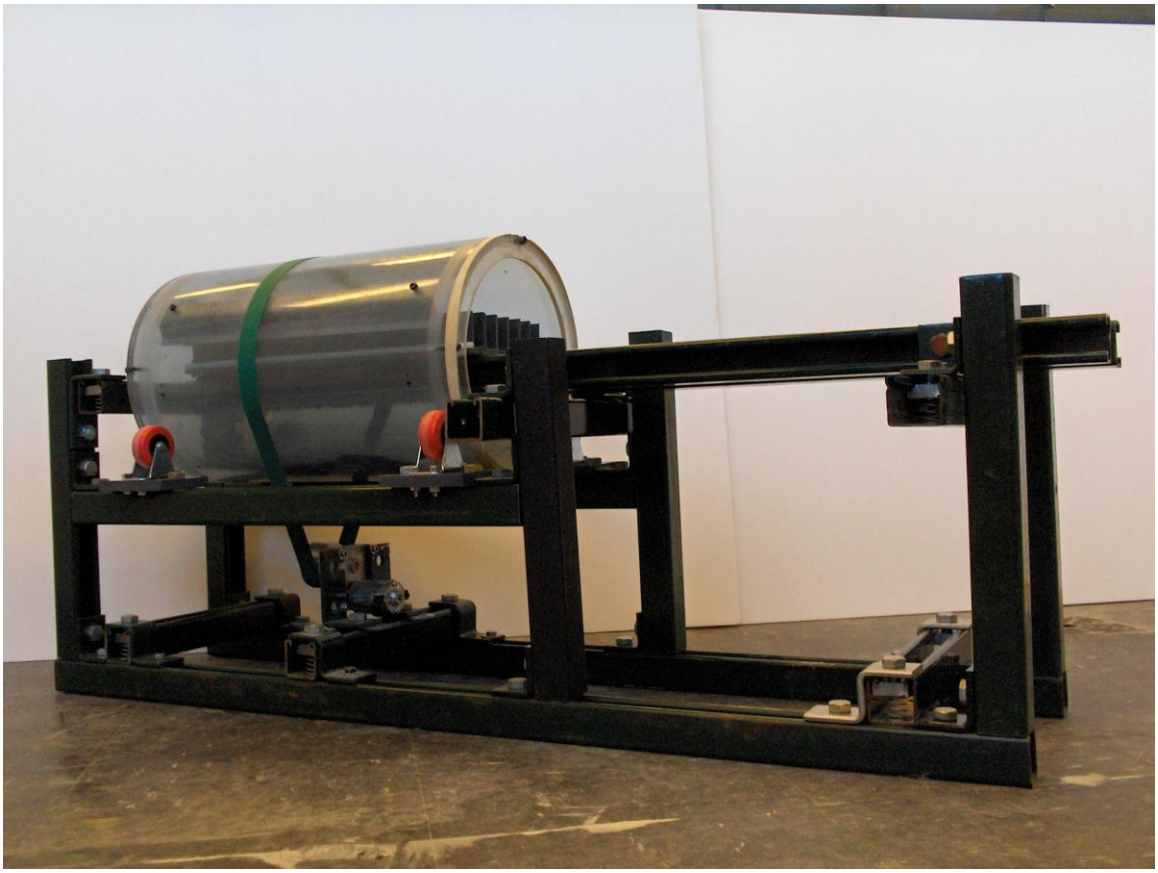

Figure 5.3 Test Rig for Sand Scoop Optimization

The array of trays was aligned with the axis of rotation and allowed measurement of the pouring distribution of various scoop configurations. The bottom of the drum was then filled with sand and rotated for testing. In this setup, a single scoop that could be quickly replaced with a new design iteration was bolted to the inside of the drum. To test a scoop's performance, the drum was rotated a set number of times to deposit sand onto the tray array. The mass of sand received by each individual tray was then measured to determine the pouring distribution. These experiments enabled rapid convergence on a sand scoop design to be used in the larger-scale prototypes. The resulting scoop design detailed in the following Figure 5.4 was employed throughout the rest of this experiment.

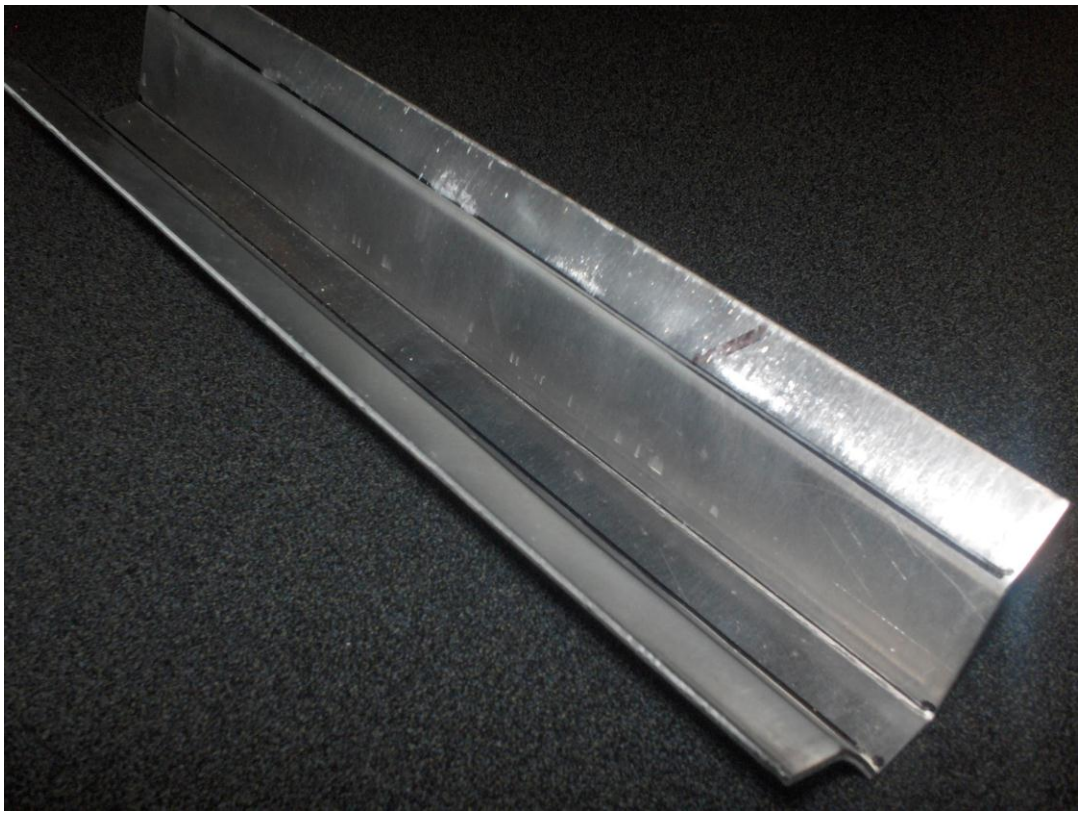

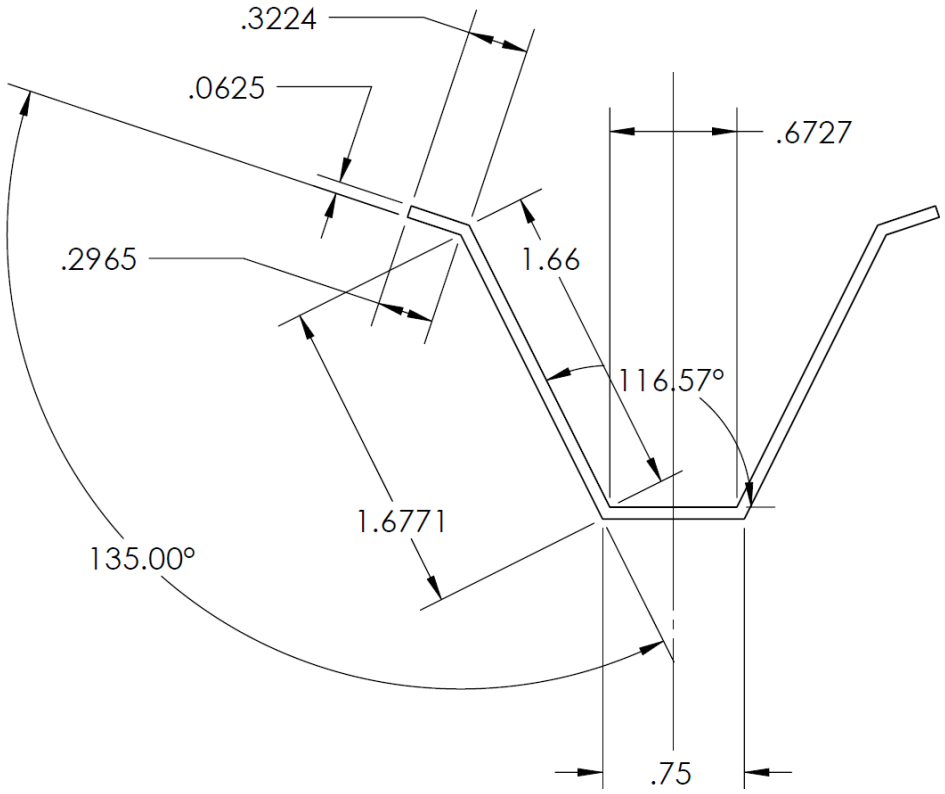

Figure 5.4 Scoop Detail View

CHAPTER 6

ROTATING DRUM HEAT TRANSFER EXPERIMENT

This apparatus, seen in Figure 6.1, as well as adjusted methodology was an improved means to allow continuous heat transfer operation over a larger range of temperatures with more realistic test articles. Here, a rotating drum with an array of internal scoops continuously lifted the sand from the bottom of the drum and poured it over an axially fitted test article.

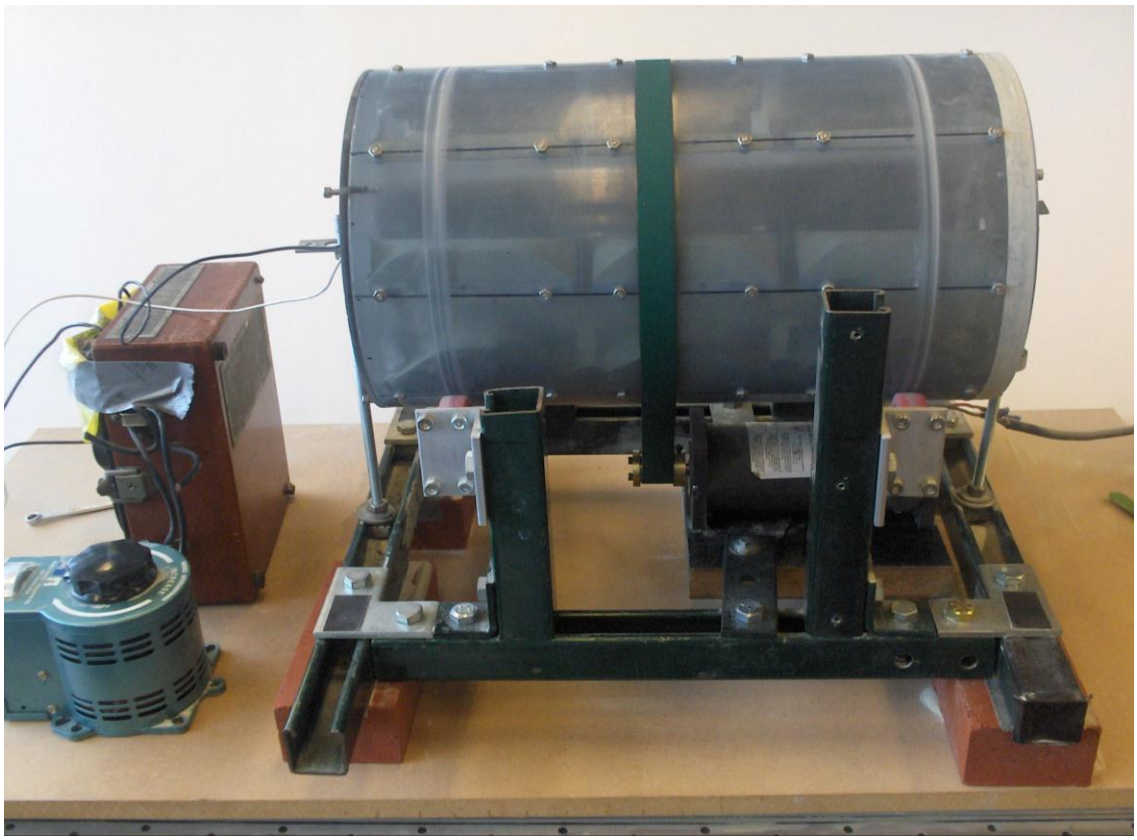

Figure 6.1 Drum Heat Exchange Measurement Apparatus

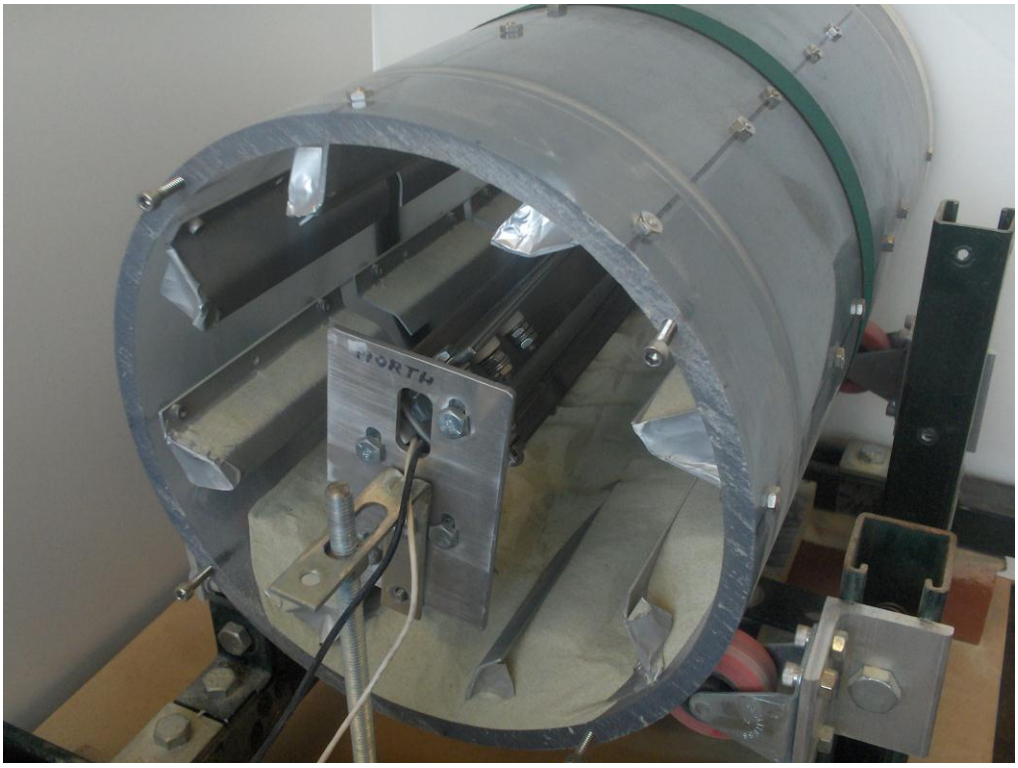

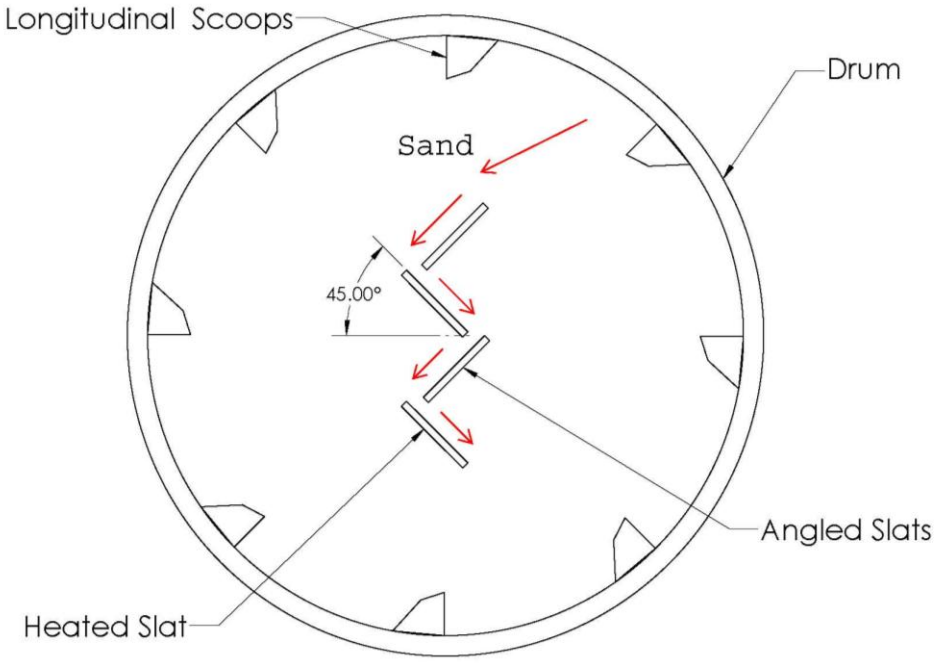

Figure 6.2 Drum Apparatus with Angled Slats

Real and Schematic View

Drum Setup

Intermittent flow was an issue for the design as the scoops only pour the sand at periodic intervals rather than continuously over the subject article as noted in Appendix C. This problem, which must also be overcome in a full size system, was alleviated by testing with an array of angled flat slats. This arrangement created a zigzag flow pattern as shown in Figure 6.2. With this flow pattern, sand was held up by internal drag, and the intermittent deposition of sand as the scoops passed over the array was quickly smoothed into a continuous flow over the lower slats. Currently, the slats are electric strip heater plates 38.1 mm wide and 336 mm in length. T-type thermocouples were mounted on the upper and lower surfaces of the lowest slat using thermal cement. Obviously, measuring any surface temperature is somewhat challenging. In this case, excellent contact between the thermocouples and the metal surface was necessary to give a reliable temperature. Welded bead thermocouples were employed for the first set of measurements. For a second confirmation measurement, the experiment was repeated with special purpose thin film thermocouples to improve the surface temperature readings. In two locations flanking the axial midpoint of the drum, rakes were suspended from the plate bundle to support the two thermocouples submerged in the sand to measure its temperature. The bottommost and most representative slat for continuous flow was then heated with a known electrical power input. The thermocouples mounted on the front and back sides measured the temperature of the sand covered surface and air cooled surface respectively. The flow speed over the slats was estimated by free body gravity analysis to be ~0.15-0.6 m/s. High speed video and image analysis software [23] looking at the sand flowing over the slat yielded a measured sand speed between, ~0.11 m/s for upper slat to around 0.17

m/s for the lower slats. Appendix D shows more detail on high speed video measurements.

Heat Leak due to Air and Heat Transfer Coefficient

Experimental runs with no sand, using only air for cooling, yielded a heat transfer coefficient for air cooling of around 10 W/m²-K. This result fell within documented range [24] of buoyant gas convection and was confirmed using the well-known formulas from McAdams [25] for heated plates. The experiment was then repeated with sand, the upper side thermocouple reading surface temperature contacted by the sand and the lower side thermocouple measuring the temperature of the slat exposed to air. The readings of the two thermocouples suspended on the rakes were averaged to return the medium temperature of the sand. Only the heated portion of the slat was exposed without insulation, with the top side covered in sand and bottom air cooled. In an experiment, the electrical input power was controlled with an autotransformer and measured with a digital power meter. The surface and sand thermocouple temperatures were measured with a scanning electronic thermometer, and the heat transfer coefficient was calculated for the sand using equation (2):

$$h_s = \frac{\dot{W}_{in} - \dot{Q}_a}{A_{sur} \cdot (T_{sur} - T_s)} \tag{2}$$

The heat transfer coefficient of sand is represented by h_s, $\dot{W}_{in}$ is the electrical power (W) input, $\dot{Q}_a$ is the estimated heat leak rate from the air side, A_{sur} the heated area (m²) covered by sand, T_{sur} is temperature (K) of the surface exposed to the sand flow, and T_s the measured sand temperature (K).

CHAPTER 7

CONVECTIVE PARTICLE PERFOMANCE ON A FLAT SURFACE

First Measurement Set: Bead Thermocouples

The newer experimental setup allowed for an improved and more realistic estimation of the heat transfer coefficient of the sand flowing over a controlled heat exchanger surface. This setup utilized bead type thermocouples to record the various surface temperatures. Exercising this arrangement with the olivine and silica sands generated measured heat transfer coefficients. The results, computed by linear regression in Excel over a range of temperature differences, are shown below in Figure 7.1.

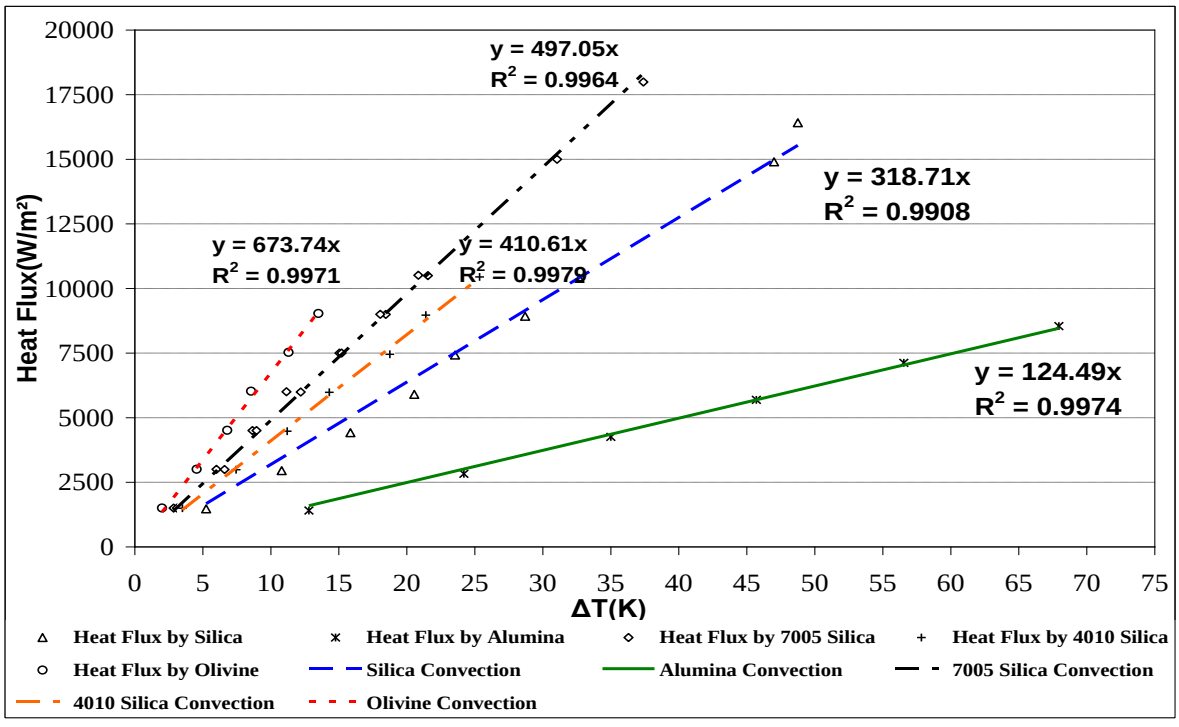

Figure 7.1 Flowing Particle Heat Transfer Data: Bead Thermocouples

The regression line slopes in Figure 7.1 indicate the average convection coefficient from the data and show a reasonable and consistent trend in temperature difference as the power input was varied. The calculated convection results with the bead thermocouples have been tabulated in Table 7.1.

Table 7.1 Heat Transfer Coefficients by Sand Type: Bead Thermocouples

Sand Type	Average Grain Size (μm)	Heat Transfer Coefficient (W/m^2-K)
Olivine Foundry Sand	80	670
Fine Sifted Silica (7005)	140	500
Sifted Silica (4010)	290	410
Construction Silica	550	320
Alumina Beads	760	125

Examination of the data shows that the particle size played a dominant role in convective performance with smaller grain sizes achieving better flowing surface contact and less internal resistance. This feature was also indicated in the literature. Observation of the experiment indicated that effective surface contact and flow continuity were the critical factors in the heat exchanger assembly evaluation. A suitable design for heat exchanger elements that effectively direct the flow of the sand will be critical to obtaining optimal thermal performance.

Second Measurement Set: Film Thermocouples

Once the experiment had been fully conducted preparations were made to fully repeat the heat transfer measurements after changing out the bead thermocouples for thin film thermocouples. The thin film thermocouples when properly adhered to a flat surface returned more accurate reading of that surfaces temperature. In short this experiment was repeated to see if the experimental results remained fairly consistent between different

means of measurement. Using this arrangement with the olivine and silica sands generated measured heat transfer coefficients. The results were calculated by regression over a range of temperature differences and are shown below in Figure 7.2 with the first set of results. Since the alumina beads proved to be so destructive, they were not re-measured with the relatively fragile thin film thermocouples.

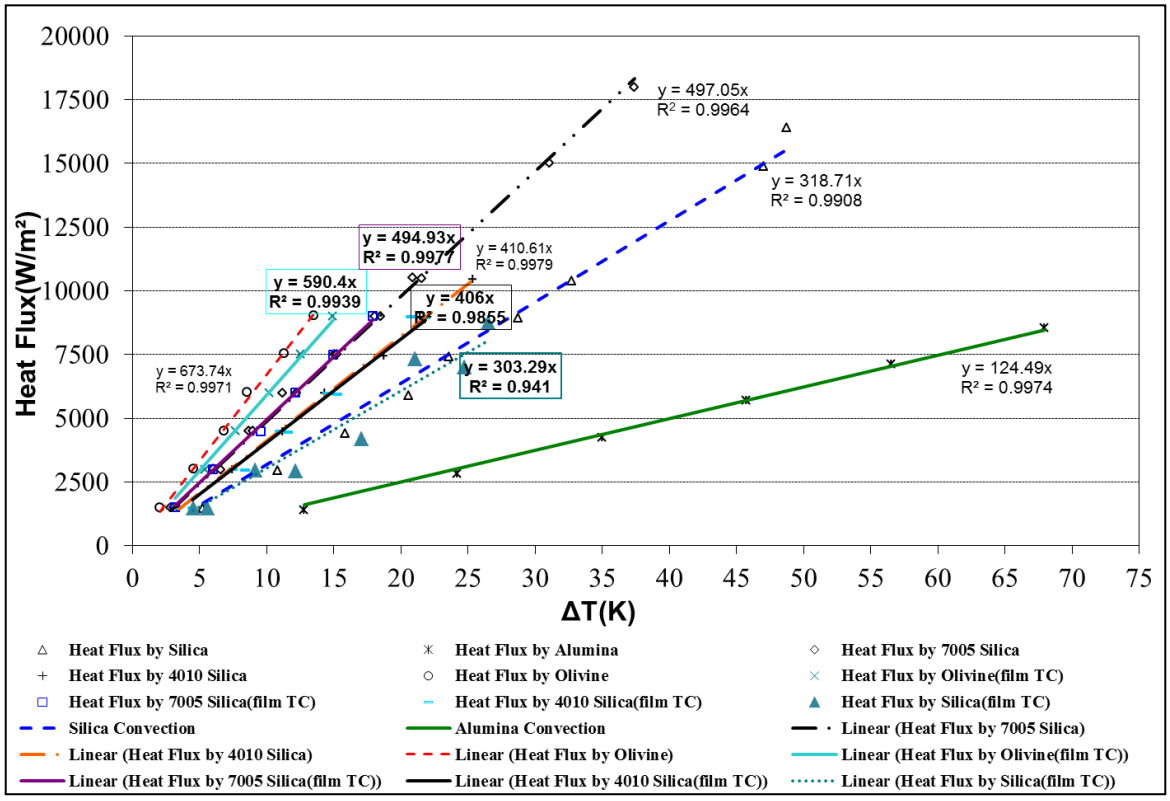

Figure 7.2 Flowing Particle Heat Transfer Data: Film Thermocouples

The regression line slopes in Figure 7.2 indicate a somewhat lower average convection coefficient from the particles. This was expected as the bead type thermocouples were more protruded into the flow from the surface and therefore experience somewhat greater cooling than the surface. The thin film thermocouples, due

to close surface profile, return a more true surface temperature when submerged in the sand flow. There was the same consistent trend in temperature difference as the power input was varied. The calculated convection results with the film thermocouples have been tabulated in Table 7.2. Examination of the data reaffirms the initial set of measurements that showed that the particle size plays the leading role in convective performance.

Table 7.2 Heat Transfer Coefficients by Sand Type: Film Thermocouples

Sand Type	Average Grain Size (μm)	Film Heat Transfer Coefficient (W/m²-K)	Bead Heat Transfer Coefficient (W/m²-K)
Olivine Foundry Sand	80	590	670
Fine Sifted Silica (7005)	140	490	500
Sifted Silica (4010)	290	410	410
Construction Silica	550	300	320
Alumina Beads	760		125

As previously indicated, grain size seems to play a major role in the convective transfer performance with smaller grain sizes achieving better flowing surface contact and better overall performance.

Error Analysis

In conducting analysis of the data it was important to examine its measured reliability. For this analysis, the focus will be on the most refined portion of the experiment, the film thermocouple results. Each component measurement came with a set uncertainty and/or assumptions. In equation (2),

$$h_s = \frac{\dot{W}_{in} - \dot{Q}_a}{A_{sur} \cdot (T_{sur} - T_s)} \tag{2}$$

$\dot{W}_{in}$ is the electrical power input (W) and was measured using an Weston analog wattmeter with a scale of 0 to 125 W. The uncertainty obtained from the instrument spec sheet was 1.25 W. This device was hooked up in series between a Variac and a heated slat to accurately measure the power input into the heater. The general setup of the experiment system and wattmeter is shown in Appendix C. It was assumed that losses were minimal between the slat and the wattmeter, and that the power delivered to the slat heater was all released as thermal energy. For the estimated loss due to air, a convection coefficient, $h_{air,}$ of 10 W/m²-K was measured in the rotating drum when run without sand. This $\dot{Q}_a$, or heat leak due to air was calculated using equation (3) assuming that the underside of the plate was exposed air with a thermocouple located on that surface $T_{back,sur}$:

$$\dot{Q}_a = h_{air} \cdot A_{sur} \cdot (T_{back,sur} - T_s) \tag{3}$$

For the loss, roughly ~5% of the total power input was spent on air cooling. The air temperature as assumed to be the same as the one measured by the sand rake thermocouples T_s. A hand held temperature probe indicated this assumption to be quite consistent. The area A_{sur} was taken as the exposed underside of the slat to the dimensions of the heated portion. The upper surface was exposed to the sand and the ends were wrapped in insulation and assumed adiabatic. A finely graduated ruler, ± 0.05 in, was used for determination of the area yielding a measurement uncertainty of 1.85E-07 m². The thermocouples were all calibrated for a range of temperatures using a standardized 4 wire RTD probe [26]. The task employed a thermocouple calibrator [27], which is a highly thermally insulated box with internal heating and temperature control. This

allowed for a finely controlled thermal range for the temperature calibration measurements.

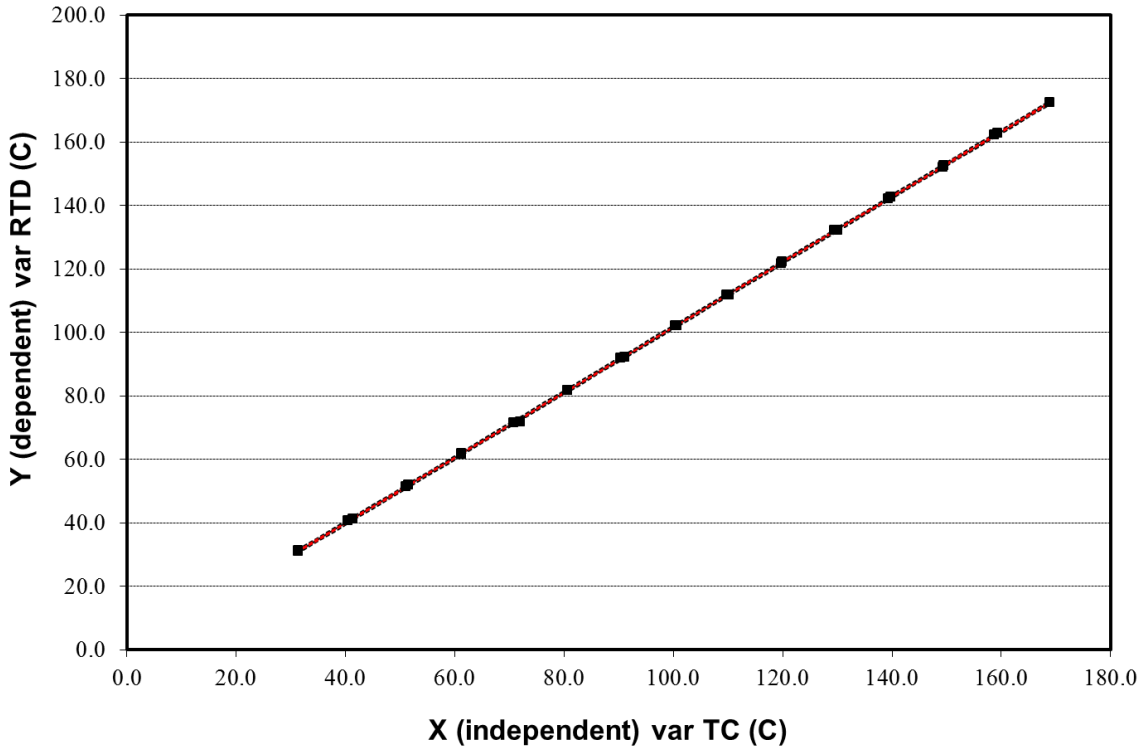

Figure 7.3 Polynomial Regression of Thermocouple and 4 Wire RTD Calibration

As indicated by Figure 7.3, the thermocouple and 4 wire RTD calibrated well, and the regression analysis yielded a distinct uncertainty for each thermocouple as well as demonstrating a close agreement for calibration. Thermocouples 2 and 3 composed the T_{sur} had a combined uncertainty of 0.0244 K. For the combined uncertainty calculation: U_a came from the regression with the RTD, in this case 0.2 and 0.24 K respectively, and the U_b from the known calibration of the SRTD was 0.02 K, Appendix F.

$$U_c^2 = U_a^2 + U_b^2 \tag{3}$$

Because U_b was so the U_c's were basically equivalent to U_b. Likewise T_s, which consisted of measurements from thermocouples 5 and 6, U_c's of 0.2 and 0.24 K, was found to have a combined uncertainty of 0.0167 K. With the component uncertainties complete, the error bias propagation for the calculation of the heat transfer coefficient was then preformed. The results for some representative cases are shown in Table 7.3 below.

Table 7.3 Heat Transfer Coefficient Error Propagation

Olivine

Measurement	U_{xi}		$\frac{\partial h}{\partial x_i}$		$U_i^2 = \left(U_{xi}\frac{\partial h}{\partial x_i}\right)^2$		Basis[a]	Source[b]
Power	1.25	W	5.22	(1/K-m²)	42.54	(W/K-m²)²	general specifications	Weston Instruments
Area	1.85E-07	m²	46985	W/K-(m²)²	7.56E-05	(W/K-m²)²	resolution	Indiced Ruler
$T_{surface}$	0.024	K	40.3	(W/m²)	0.967	(W/K-m²)²	calibration	see note (1)
T_{sand}	0.017	K	40.3	(W/m²)	0.450	(W/K-m²)²	calibration	see note (1)
Total $(U_b)^2$					42.55	(W/K-m²)²		

Fine Sifted Silica (7005)

Measurement	U_{xi}		$\frac{\partial h}{\partial x_i}$		$U_i^2 = \left(U_{xi}\frac{\partial h}{\partial x_i}\right)^2$		Basis[a]	Source[b]
Power	1.25	W	4.35	(1/K-m²)	29.61	(W/K-m²)²	general specifications	Weston Instruments
Area	1.85E-07	m²	39128	W/K-(m²)²	5.24E-05	(W/K-m²)²	resolution	Indiced Ruler
$T_{surface}$	0.024	K	28.0	(W/m²)	0.467	(W/K-m²)²	calibration	see note (1)
T_{sand}	0.017	K	28.0	(W/m²)	0.217	(W/K-m²)²	calibration	see note (1)
Total $(U_b)^2$					29.62	(W/K-m²)²		

Note(1): Standardized 4 Wire RTD Probe, see Appendix F

Table 2.3 Heat Transfer Coefficient Error Propagation

Sifted Silica (4010)

Measurement	U_{xi}		$\frac{\partial h}{\partial x_i}$		$U_i^2 = \left(U_{xi}\frac{\partial h}{\partial x_i}\right)^2$		Basis[a]	Source[b]
Power	1.25	W	5.37	(1/K-m²)	44.99	(W/K-m²)²	general specifications	Weston Instruments
Area	1.85E-07	m²	31970	W/K-(m²)²	3.50E-05	(W/K-m²)²	resolution	Indiced Ruler
$T_{surface}$	0.024	K	28.2	(W/m²)	0.474	(W/K-m²)²	calibration	see note (1)
T_{sand}	0.017	K	28.2	(W/m²)	0.221	(W/K-m²)²	calibration	see note (1)
Total $(U_b)^2$					45.00	(W/K-m²)²		

Construction Silica

Measurement	U_{xi}		$\frac{\partial h}{\partial x_i}$		$U_i^2 = \left(U_{xi}\frac{\partial h}{\partial x_i}\right)^2$		Basis[a]	Source[b]
Power	1.25	W	3.15	(1/K-m²)	15.53	(W/K-m²)²	general specifications	Weston Instruments
Area	1.85E-07	m²	22057	W/K-(m²)²	1.67E-05	(W/K-m²)²	resolution	Indiced Ruler
$T_{surface}$	0.024	K	11.4	(W/m²)	0.078	(W/K-m²)²	calibration	see note (1)
T_{sand}	0.017	K	11.4	(W/m²)	0.036	(W/K-m²)²	calibration	see note (1)
Total $(U_b)^2$					15.54	(W/K-m²)²		

Note(1): Standardized 4 Wire RTD Probe, see Appendix F

As can be seen in Table 7.3, the total bias uncertainty, U_b, was ~6.5 W/K-m² for olivine, ~5.4 W/K-m² for fine sifted silica, ~6.7 W/K-m² for fine silica, and ~3.9 W/K-m² for construction silica. Regression analysis was performed on the flux, ΔT plot for the heat transfer coefficient to get the random uncertainty, U_a, which was the average of the difference for the upper and lower 95% band. The regression plots for each sand type are found in Appendix G and the uncertainties have been tabulated below in Table 7.4.

Table 7.4 Regression Analysis of Heat Transfer Coefficients and Combined Uncertainty

Sand Type	Coefficient (W/K-m²)	U_a (W/K-m²)	U_b (W/K-m²)	U_c (W/K-m²)
Olivine	590	13	6.5	15
Fine Sifted Silica	490	12	5.4	13
Fine Silica	410	20	6.7	22
Construction Silica	300	34	3.9	34

For the uncertainties, the random uncertainty dominates in the calculation for total uncertainty, U_c, equation 3. It should be noted that the course construction silica was by far the least homogeneous of the sand types tested and may explain the higher random variance. Overall the heat transfer coefficients measured by this experiment, providing the assumptions of adiabatic insulation, cooling by air, and total coverage of only the upper surface by sand, have a measurement reliability to within ~10% or less of the stated value. This level of uncertainty is well within the range typically expected in heat transfer engineering applications.

CHAPTER 8

MEASUREMENT COMPARISON AND ANALYSIS

Literature Model Comparison

Of the literature on particulate flow that we have reviewed, the work reported by Patton et al. [16] appears to be the most suitable resource for comparing with our empirical results. The convective heat transfer coefficient of flowing sand was modeled with the relations found in that paper [16] to compare the published results with the heat transfer coefficient determined experimentally. The parameters in the equation based model included particle size, conductivity, specific heat, flow velocity, layer thickness, and packing ratio (ratio of air space vs. solid space). From this data a heat transfer coefficient range was determined for several types of particles. For the particle types, the following parameters were used: (1) Fine grained olivine sand [28], experimentally measured to have a mean diameter of 80 μm with a standard deviation 30 μm. (2) A slightly larger finely sifted silica [29] measured to have a mean diameter of 140 μm with a standard deviation of 50 μm. (3) Another sifted silica [29] sand measured to have a mean diameter of 290 μm with a standard deviation of 100 μm. (4) A coarser locally purchased construction silica sand was measured to have a mean diameter of 550 μm with a standard deviation of 320 μm. (5) Finally spherical alumina particles [30] measured to have a mean diameter of 760 μm with a standard deviation of 120 μm. Additionally, the velocity of the particle layer was estimated to be between 0.1~0.3 m/s, Appendix D, the thickness of the layer to be 0.4 mm to 2 mm, and the packing ratio (volume of solid material vs. total volume of sample) between 0.2 and 0.42. Using these

parameters in the EES [19] model the produced convective heat transfer coefficient ranges as listed in Table 8.1 as well as model figures showing the measurement bounded by the model predicted ranges.

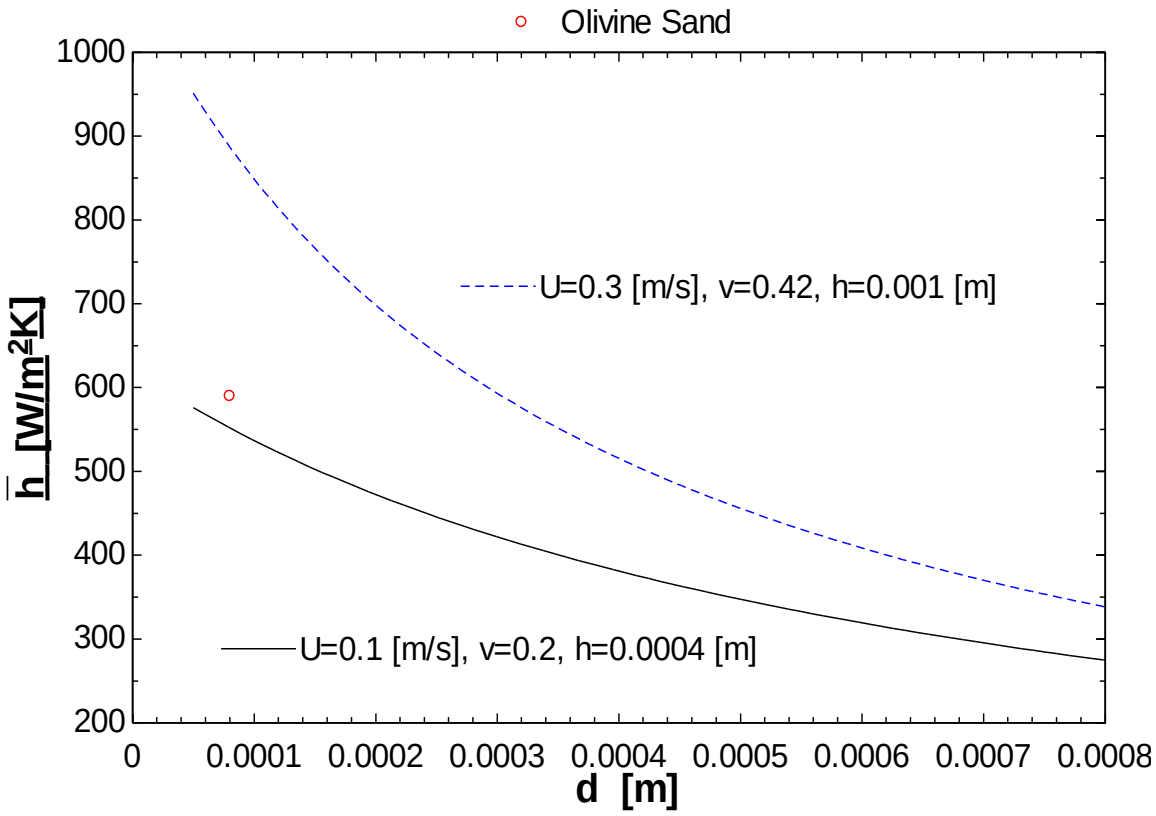

Figure 8.1 Model and Measurement Comparison for Olivine Sand

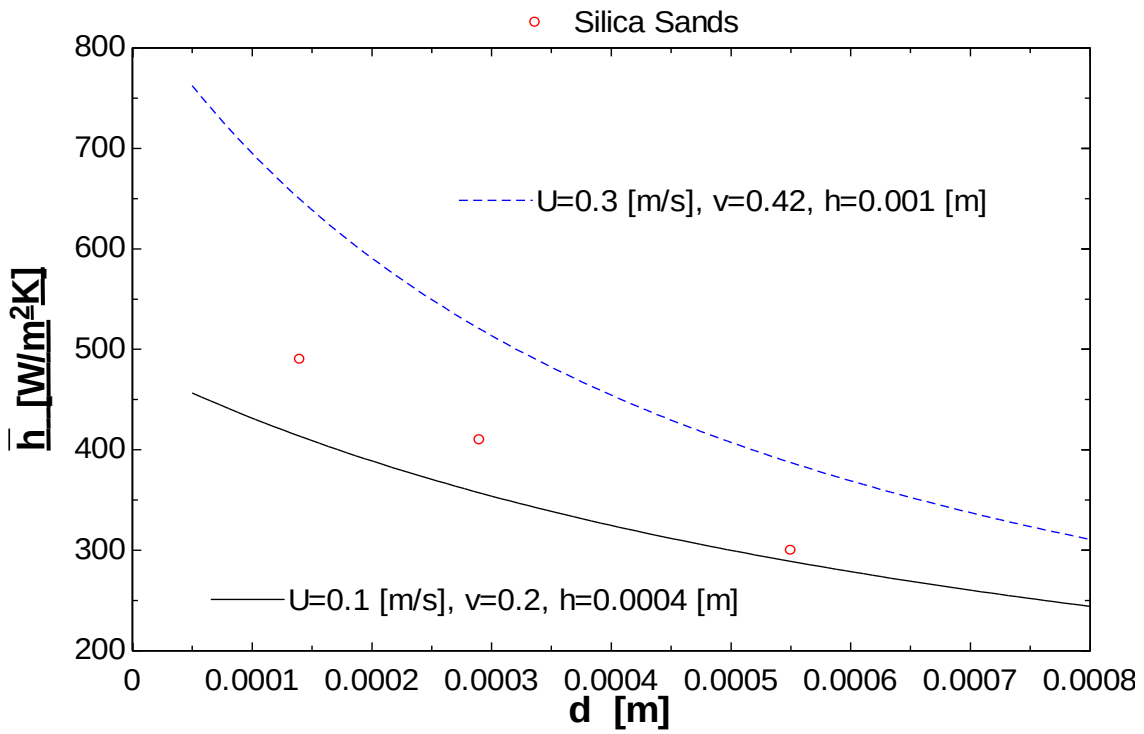

Figure 8.2 Model and Measurement Comparison for Silica Sands

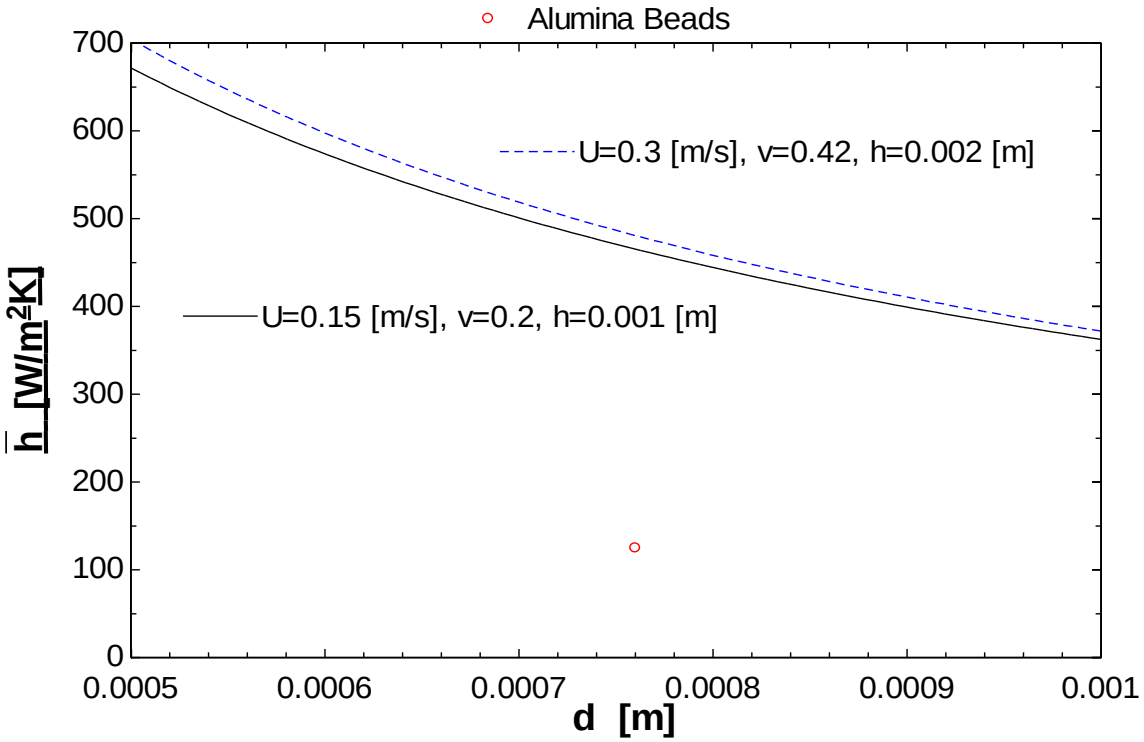

Figure 8.3 Model and Measurement Comparison for Alumina Beads

Table 8.1 Modeled Heat Transfer Coefficient by Particle Type

Sand Type	Model Heat Transfer Coefficients (W/m²-K)	Heat Transfer Coefficient (W/m²-K)	Average Grain Size (μm)
Olivine	552-887	590	80
Fine Sifted Silica	413-649	490	140
Sifted Silica	357-520	410	290
Regular Silica	289-387	300	550
Alumina Beads	465-481	125	760

Of the materials measured, all except the alumina fell within the modeled range. The model is influenced by the enhanced conductivity and specific heat of alumina leading to the higher predicted heat transfer coefficient despite the larger particle size. Experimentally, however, the alumina spheres tended to bounce instead of flowing when dropped on the slat surface. This reduced the period of surface contact and may explain the lower measured convective coefficient by altering the contacted area assumption. In addition, it should be noted that even at these low speeds the alumina beads produced noticeable wear on the heat exchanger surfaces, a problem that must be avoided in service.

The experimental results found in this paper of around 590 W/m^2-K for olivine sand and around 300-500 W/m^2-K for silica sand generally fall within the ranges predicted by the model. In comparison to empirical literature results Denloye, et. al. [14] measured maximum heat transfer coefficients of ~310 W/m^2-K for 590 μm sand and ~475 W/m^2-K for 160 μm sand which fit with the experimental results in this thesis. Similarly Hyde, et. al.'s [15] fluidized bed measurements for heat transfer coefficients showed ~300 W/m^2-K for 560 μm sand, ~360 W/m^2-K for 450 μm sand, ~405 W/m^2-K for 295 μm sand, and ~450 W/m^2-K for 225 μm sand. The relative agreement of these

results suggest that treating a thinly flowing layer of sand as a fluidized bed it not an unreasonable assumption for heat transfer coefficient estimation purposes. Of the factors that affect the heat transfer, particle size has the dominant effect on the heat transfer coefficient followed by velocity, layer thickness, and packing ratio. The Babcock and Wilcox report [17] that looked into a range of TES options indicated a convection coefficient on their heat transfer elements of around 930-1160 W/m^2-K using a moving bed of sand. The sand utilized in Babcock and Wilcox report [17] had a grain size of 44-77 μm, a packing ratio of 0.42, and a sand velocity around 0.15-0.3 m/s, which was near the conditions of the olivine sand of the current experiment. While this earlier report suggests that high heat transfer performance can be achieved with very fine sand, limited experimental details were given; and our experimental results do project heat transfer coefficients lower than those reported and used in the 1981 report [17].

Conclusion

This experiment, after some refinement, was able to measure the heat transfer coefficient between flowing particulate sand and a generic heat exchanger surface. The resulting coefficients indicate that smaller particle size plays a major role in improving heat exchange. Of particular interest is that ordinary silica sand in finer grain size performs about as well as the slightly more exotic olivine sand. It is also notable that the alumina beads, despite the potential advantage of slightly higher specific heat and significantly greater thermal conductivity as well as density, have poor performance and high errosiveness. The poor performance is evidently because of the highly elastic rebound after impact consequently caused poor maintenance of contact with the heated surface, in short the alumina tended not to “flow” along the angled surface resulting in

the depressed heat transfer coefficient. These factors and overall higher cost hamper its potential as a viable particulate heat storage medium. For the silica sands, a smaller grain size is highly desirable, and continuous flow with good surface contact will be critical for high performance with any sands or particulate mediums. While it may be reasonable for estimation treating a thin layer of flowing sand as comparable to a fluidized bed, the heat transfer of sand or other particulates is definitely contingent on a wide range of conditions. As a result it is recommended that experimental measurement of particulates be taken on a case by case basis.

APPENDIX A

HEAT TRANSFER MODEL

In Patton's model [16] the convective heat transfer coefficient is calculated by:

$$\bar{h} = \frac{k_g \overline{Nu_d^*}}{d} \tag{4}$$

Where K_g is the conductivity of the gas, d is the particle diameter and $\overline{Nu_d^*}$ is the Nusselt number calculated by:

$$\overline{Nu_d^*} = \left[\chi + \frac{\sqrt{\pi}}{2}\frac{1}{\sqrt{Pe_L^*}}\left(1 + \beta\frac{Fr^*}{\sqrt{Pe_L^*}}\right)\right]^{-1} \tag{5}$$

Where χ and β are taken to be empirical constants for this model, and Pe_L^* and Fr^* are the Péclet and Froude numbers respectively defined as:

$$Pe_L^* = \frac{UL}{\alpha}\left(\frac{d}{L}\right)^2\left(\frac{k}{k_g}\right)^2 \tag{6}$$

$$Fr^* = \frac{U^2}{gh\cos\theta}\frac{v_c}{v}\frac{k}{k_g}\frac{d}{L} \tag{7}$$

Where U is the flow velocity, L is the length of the heated plate, α is the thermal diffusivity of the sand, k is the conductivity of the sand, g is gravitational acceleration, h is the thickness of the sand layer, v is the solid fraction, and v_c is the critical solid fraction (an empirical constant).

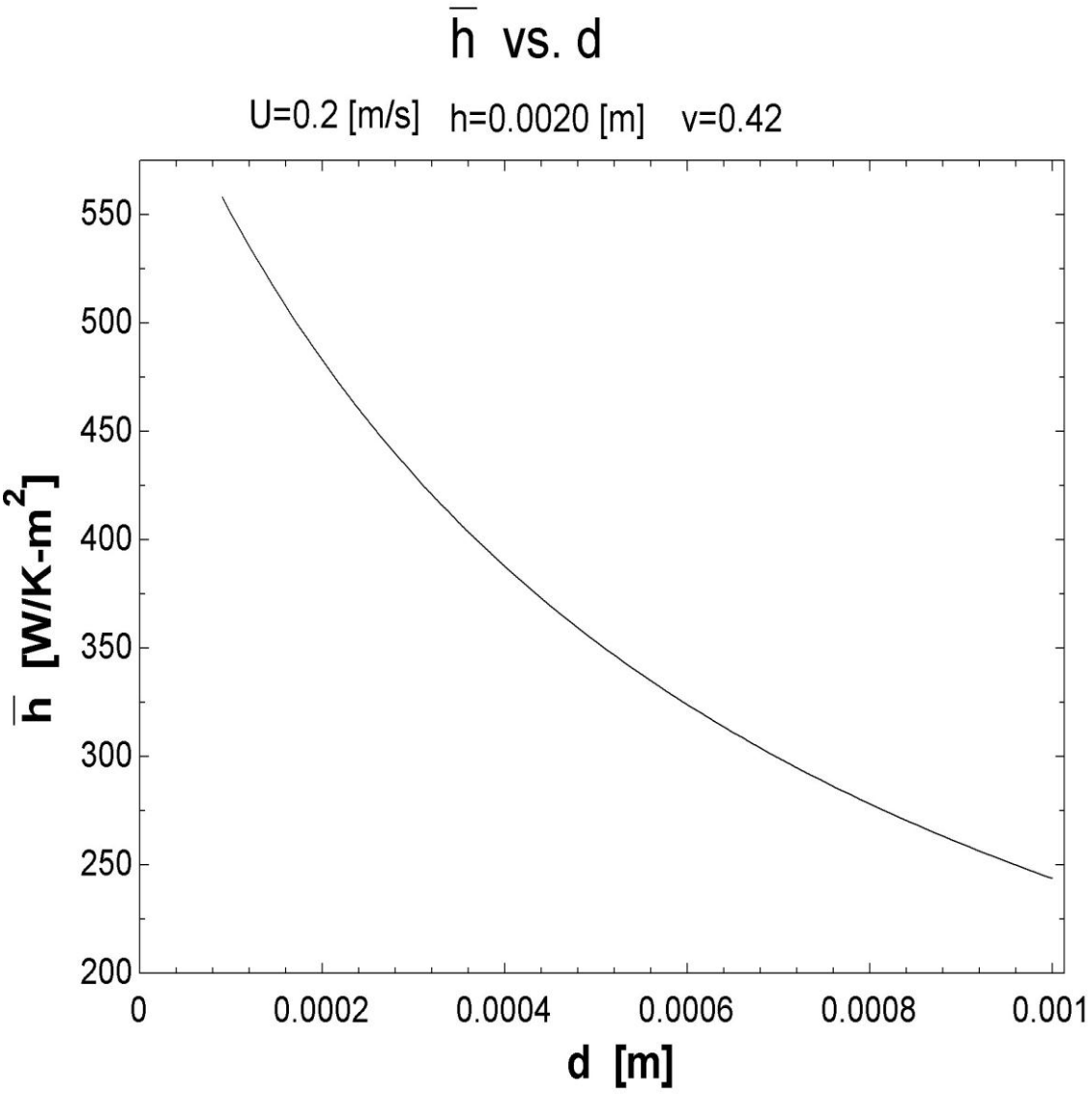

Figure A.1: Convection Coefficient vs. Particle Diameter

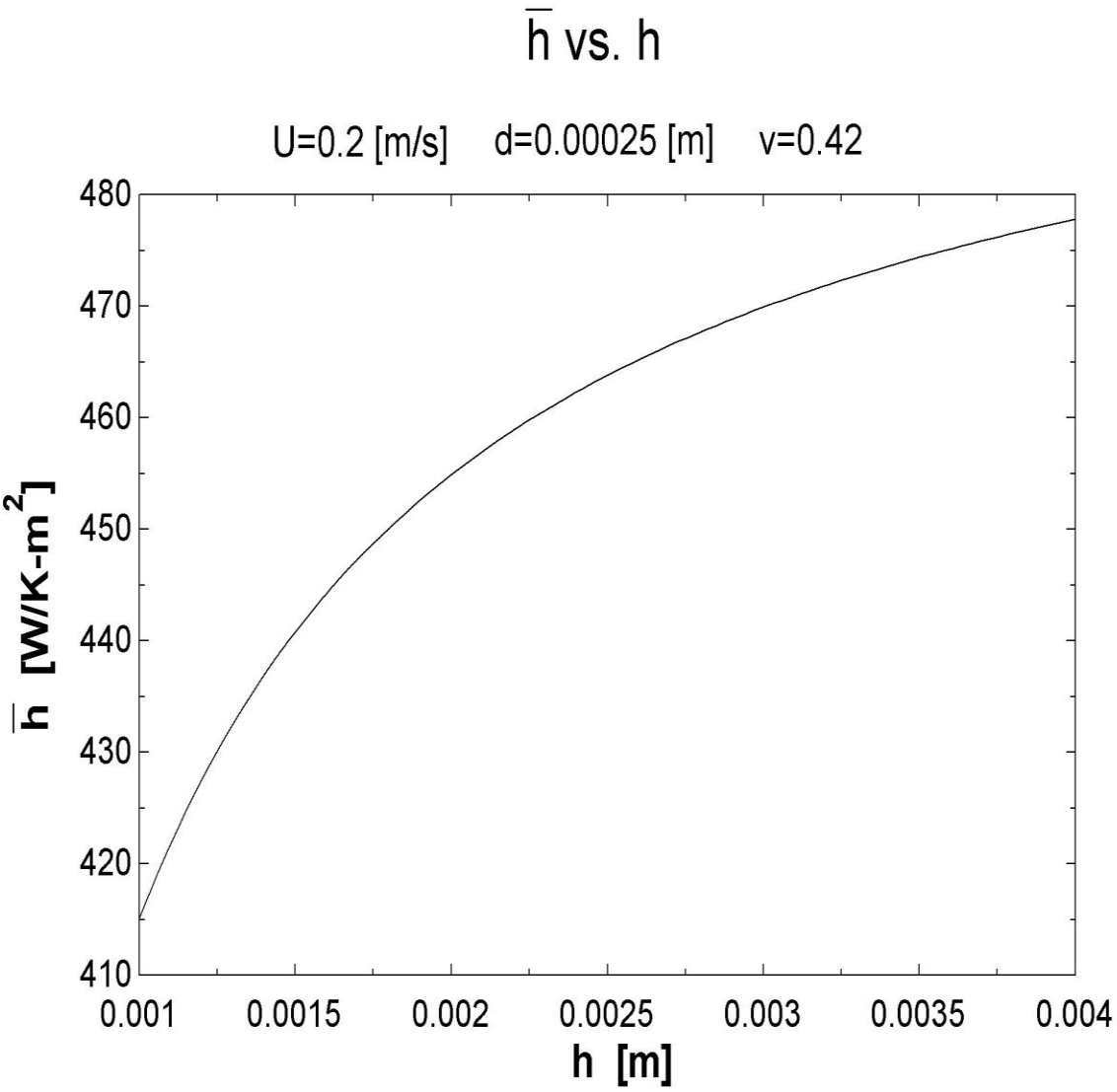

Figure A.2: Convection Coefficient vs. Layer Thickness

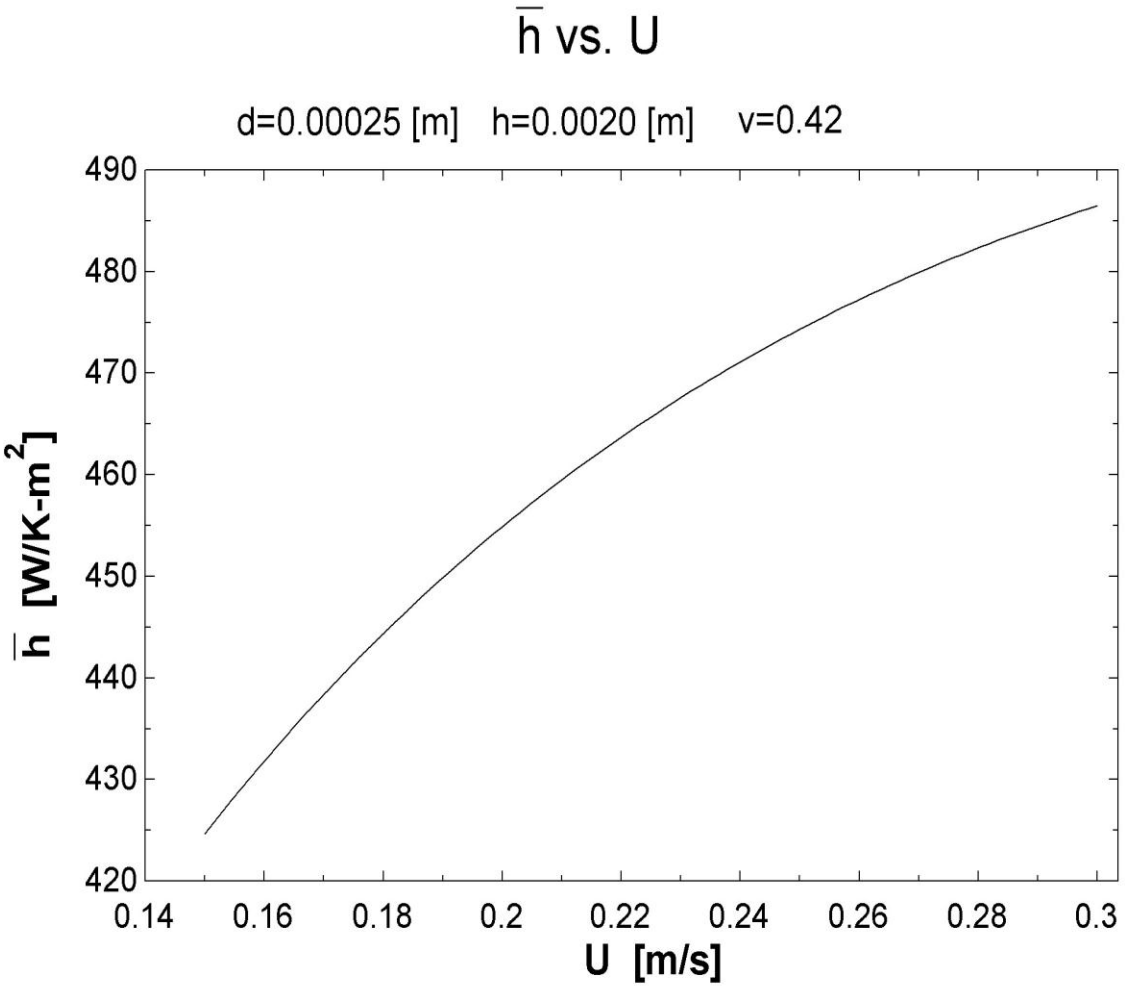

Figure A.3: Convection Coefficient vs. Flow Velocity

APPENDIX B

GRAIN SIZE MEASUREMENTS

Realistic and reliable particle diameters are needed and are critical in the models, and standard sieve tests do not seem to generate precise results adaptable to simple statistical analyses especially for irregular particles. Consequently, it was decided to use a somewhat exhaustive direct visual examination of the grain size measurements. This observation was performed using a microscope adapted to record video. The video was allowed to roam over a large sample dish containing the particulate material. The video was then analyzed to measure the grains approximate diameters and determine and average grain size as well as deviation. The following pictures are example frames from the videos, the table contains the measurements.

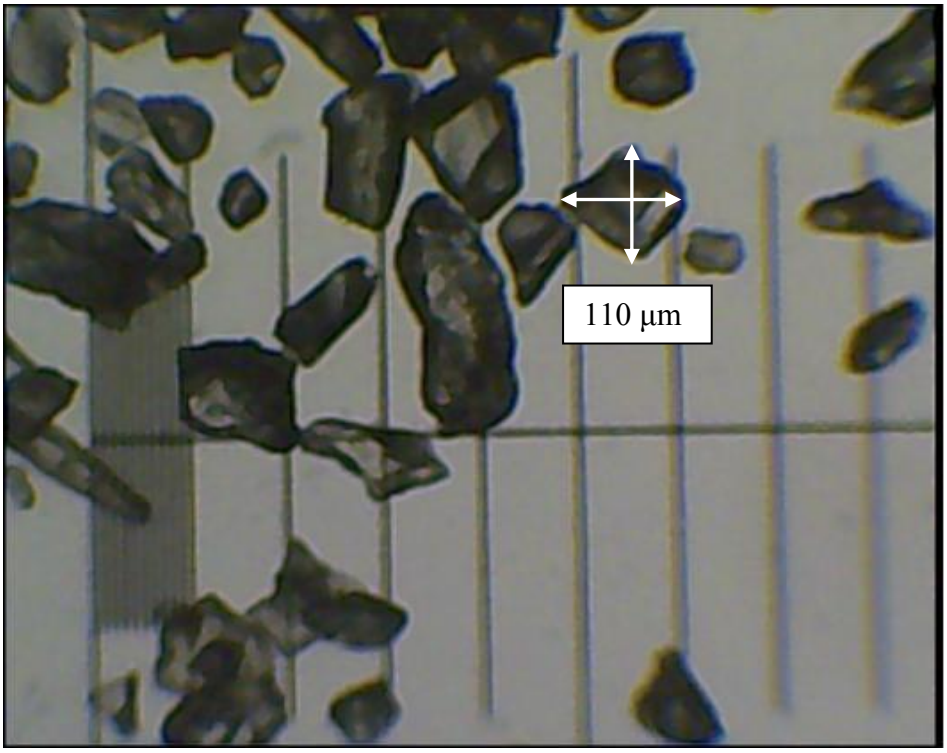

Figure B.1: Olivine Sand

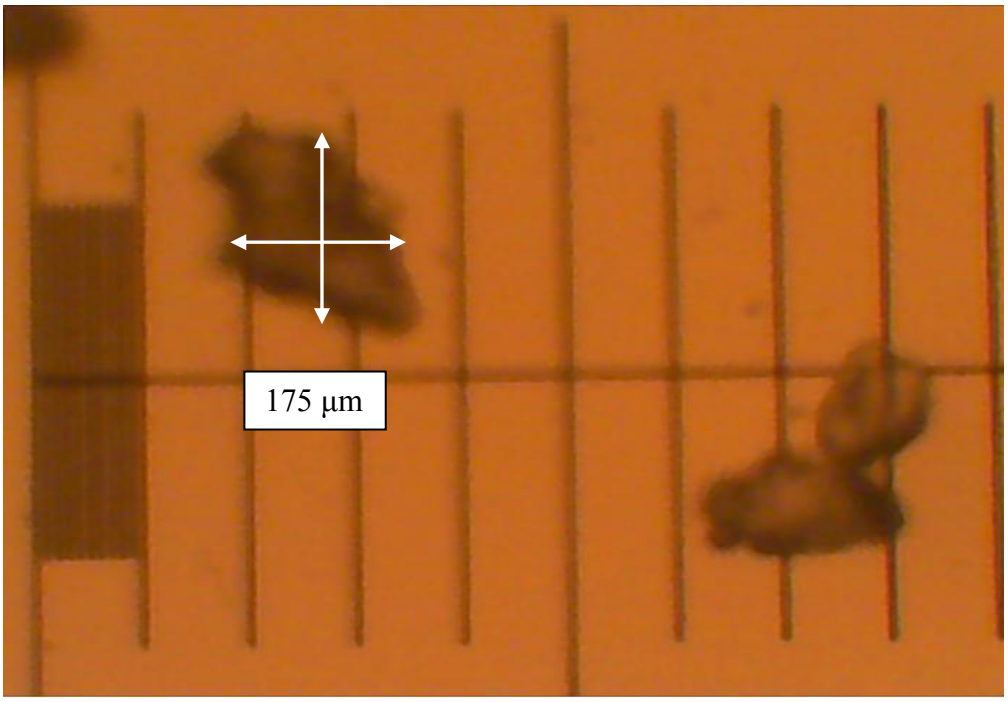

Figure B.2: Fine Sifted Silica, Granusil 7005

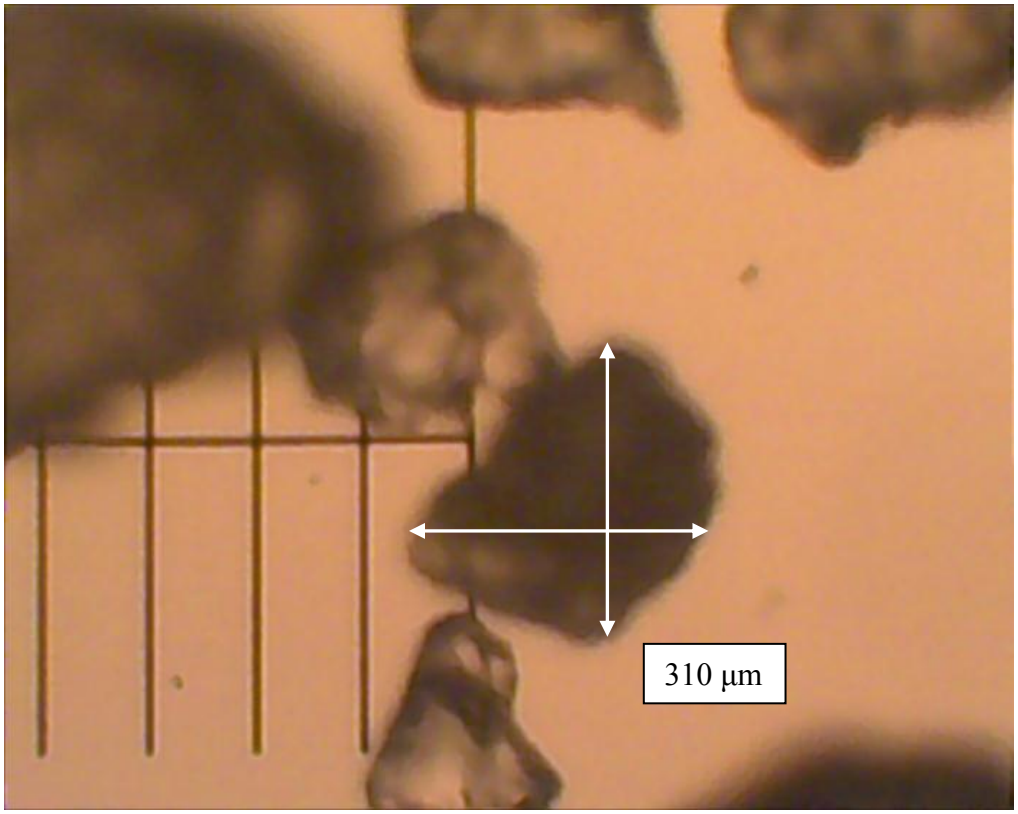

Figure B.3: Fine Silica, Granusil 4010

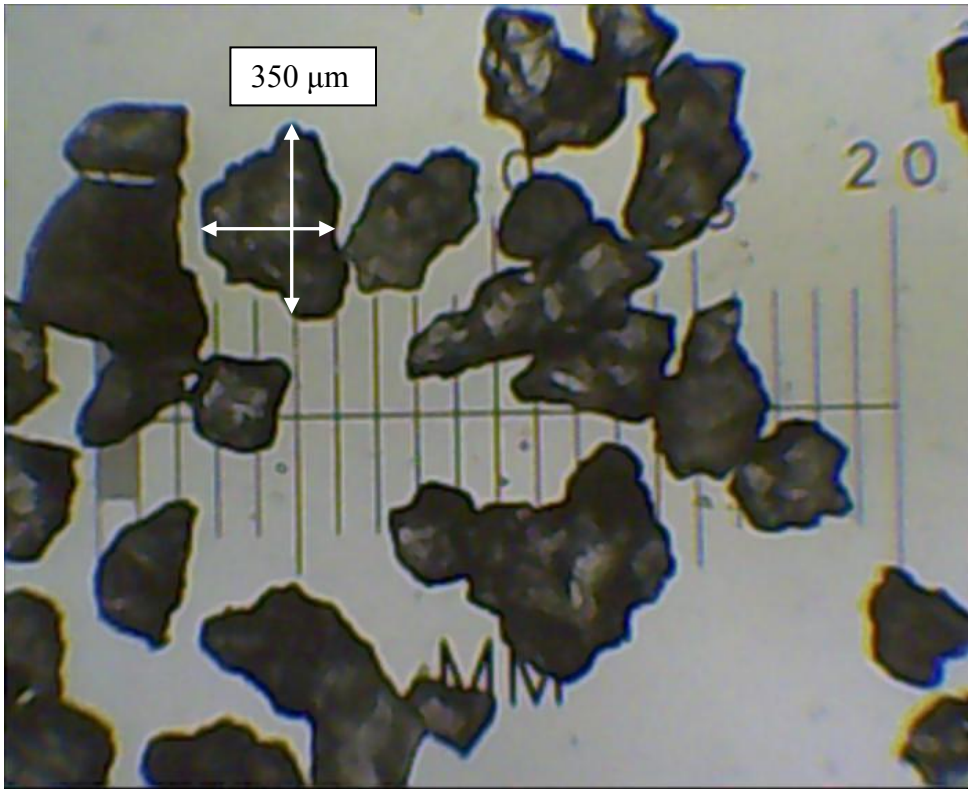

Figure B.4: Silica Sand

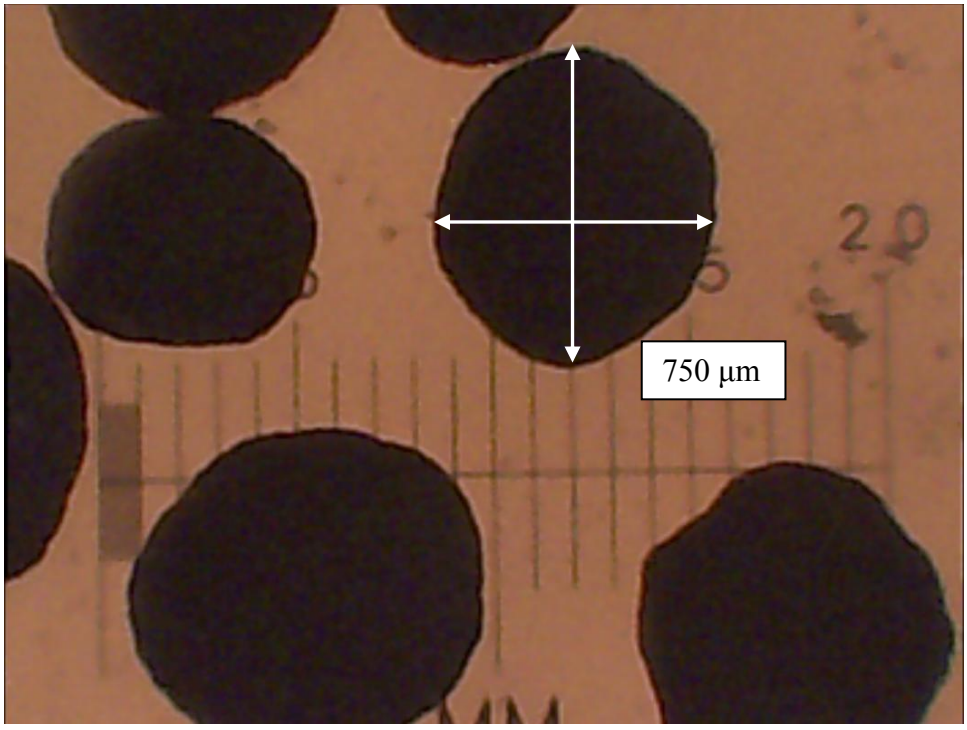

Figure B.5: Alumina Beads

Table B.1: Grain Size Measurements

	Olivine [0.01 mm]		Granusil 7005 [mm]		Granusil 4010 [mm]		Silica [mm]		Alumina [mm]	
	diameter	s	Count	diameter	Count	diameter	diameter	s	Count	diameter
	8.5		3	0.200	5.25	0.350	1.4	0.1		0.900
	5		2.5	0.167	8	0.533	0.4	0.05		0.800
	7		1.75	0.117	3.75	0.250	0.6	0.1		0.700
	13		1.75	0.117	5	0.333	0.4	0.03		0.600
	11		1.75	0.117	7	0.467	0.8	0.1	5	0.750
	5		1.75	0.117	3.5	0.233	0.6	0.1	4	0.600
	11		2	0.133	3	0.200	0.6	0.1	4.5	0.675
	6		1.5	0.100	4.5	0.300	0.4	0.5	4	0.600
	5		2.25	0.150	3.25	0.217	0.3	0.25	6	0.900
	12		1.75	0.117	3	0.200	0.65	0.5	4.5	0.675
	5		1.75	0.117	2.5	0.167	0.25	0.05	5.5	0.825
	5		2	0.133	4	0.267	0.2	0.025	6	0.900
	10	1	2	0.133	4.5	0.300			4.5	0.675
	10	1	3.75	0.250	8.25	0.550			5	0.750
	7	0.5	3.75	0.250	3	0.200			7	1.050
	9	0.25	1.5	0.100	4	0.267			5	0.750
	2	0.25	1.75	0.117	5.75	0.383			5	0.750
	10	0.5	2	0.133	3.25	0.217			6.5	0.975
	5	1	1.5	0.100	5.5	0.367			5	0.750
	9	7	1.75	0.117	3.5	0.233			5	0.750
			2.5	0.167	3.5	0.233			4.5	0.675
			1.5	0.100	2.5	0.167				
			1.25	0.083	4	0.267				
			1.5	0.100	3	0.200				
			3.75	0.250	3.75	0.250				
					5	0.333				
Average:	0.078			0.139		0.288	0.550			0.764
St. dev.:	0.030			0.049		0.104	0.323			0.123

APPENDIX C

MEASUREMENT OF HEATED FINNED TUBE ASSEMBLY

A**bstract**

The purpose of this experiment was to ascertain an approximate convective heat transfer between a heated tube with annular fins and sand being continuously poured over the tube. This was accomplished by means of suspending the heated tube in center of a rotating drum. The drum was fitted with scoops set at 45 degree intervals so when the drum was filled with sand and when rotated would ensure flow of sand over the heated tube. The ends of the drum were closed with a central hole just large enough to allow for the tube and fins to limit sand leakage. The tube was heated by means of an electrical heater wire suspended in the concentric center of the tube in mineral oil. This setup with the wire and oil fluid helped ensure a more uniform heated tube fin assembly. Being electrically heated an exact power input reading could be measured for the tube. A pair of thermocouples located on the surface of the tube and a pair suspended on rakes in the drums sand measure the tube and sand temperature respectively. A DC motor employing a belt drive was used to rotate the drum assembly.

As detailed below, the heat transfer performance of this finned-tube design was found to be substantially lower than the corresponding flat plate performance obviously because of the poor contact between the sand and the tubes and the nearly vertical fins. The measured convection coefficients are an order of magnitude less than the corresponding flat plate results, this is likely due to the intermittent flow of sand over the test article which would contribute greatly to the poor period of sand contact.

Methodology

For measurement, the input power was set and the system allowed to sit for 30 minutes to reach a steady state. Then the DC motor was engaged to start the heat transfer between the pouring sand and finned tube. Steady state was reached after about 10-15 minutes with temperature readings from the thermocouples taken leading up and including the steady state point. With a known power input, measured tube temperature, measured sand temperature and known surface area of the finned tube a convection value was estimated. A key note for this was that though the surface area of the tube and fins were known, the area actually in contact with the pouring sand was significantly less so the resulting estimation is quite conservative.

Measurements

Using the above stated method, the data for three separate runs at different input power was run and recorded. The input dial for the DC motor was set to ~3.2 with a resulting rotation of 11-12 rpm. The variance was due to the drum being driven with a belt which was susceptible to slip.

Table C.1: Sand/Finned Tube Convection Data (80W)

	Tube Sensors, C				Sand Sensors, C			
	T1	Ave	T2	Delta T	T3	Ave	T4	RPM
80W	95.3	97.8	100.2	63.2	34.6	34.6	34.6	11(~3.2)
2 min	54.6	55.0	55.3	12.3	42.7	42.7	42.7	
4 min	49.7	49.8	49.9	7.4	42.2	42.4	42.6	
6 min	48.4	48.4	48.4	6.3	42.0	42.1	42.2	
8 min	47.9	48.0	48.0	6.0	41.8	42.0	42.1	
10 min	47.7	47.8	47.8	5.9	41.7	41.9	42.0	
13 min	47.6	47.7	47.8	5.9	41.7	41.8	41.9	

Table C.2: Sand/Finned Tube Convection Data (120W)

	Tube Sensors, C				Sand Sensors, C			
	T1	Ave	T2	Delta T	T3	Ave	T4	RPM
120W	120.5	124.0	127.4	84.3	39.2	39.7	40.2	12(~3.2)
2 min	69.4	70.3	71.1	18.6	51.2	51.7	52.1	
4 min	62.6	63.1	63.5	11.8	50.9	51.3	51.6	
6 min	60.7	61.1	61.4	10.2	50.5	50.9	51.2	
8 min	60.1	60.6	61.0	10.0	50.3	50.6	50.9	
10 min	60.1	60.6	61.0	9.9	50.3	50.7	51.0	
13 min	60.4	60.9	61.3	10.1	50.4	50.8	51.2	

Table C.3: Sand/Finned Tube Convection Data (162W)

	Tube Sensors, C				Sand Sensors, C			
	T1	Ave	T2	Delta T	T3	Ave	T4	RPM
162W			Sensor was in flux					12(~3.2)
				T1-Ave34				
2 min	79.0		111.0	23.4	53.8	55.6	57.4	
5 min	66.7		100.5	10.4	55.2	56.3	57.4	
8 min	66.0		98.4	9.6	55.7	56.5	57.2	
10 min	67.1		97.6	10.4	56.1	56.7	57.3	
13 min	67.0		96.0	9.9	56.6	57.1	57.6	

In the third run, Table C.3, thermocouple 2 was unstable returning wildly shifting readings, and was likely damaged. What was recorded was an estimated average between the high and low ends at the time of measurement. Thermocouple 1 remained fairly stable and was used as it remained consistent with the prior two runs. Using the conservatively estimated thermal interaction surface area, the temperature difference between the tube and the sand rakes, as well as the known power input a convection estimate was calculated. The resulting range was ~45-60 W/m^2-K which put it out of the range of convection by air and on the low end of standard liquid convection region [24].

Summary

Further refinements such as more accurately determining the "wetted" contact area are needed to get a more exact measure of the convective properties of the sand. A design that lets the sand effectively cover the surfaces continuously will be crucial. The next design refinements planned will entail using flat electrically heated strips offset at angles as to catch and direct sand raining down it onto a strip below it. With this, a more

exact contact zone can be ascertained, but there is somewhat of a trade off with the use of multiple strips as each will be at a different temperature, the top being the coolest the bottom the warmest. The strips may be treated piece wise, with an average temperature from surface thermocouples for each heated slat area employed.

APPENDIX D

SAND VELOCITY MEASUREMENT

The sand velocity measurements were taken utilizing a high speed camera [31]. The video was then loaded into the Logger Pro [23] software. Using this software tool allowed analysis to be easily done frame by frame with a time stamp. With the software, length measurements could simply be done in the video using a pre-measured reference standard. With a measurable reference length in the video and high speed frame time stamps, a velocity could be ascertained by following distinct features in the sand flow frame by frame over a distance in the video. In addition there were two types of sand available for use of the same grain size, a light color type and a dark variant. For some measurement cases, layering the different color sands in a dispensing funnel created a distinct visual feature that could be more easily tracked. These measurements yielded a sand flow speed of ~0.11 m/s for upper slat and ~0.17 m/s for the lower slats. The following figures show some representative velocity measurement frames. There were two primary camera views used in measurements, an end on view and a normal view.

Currently these measurements have relied on visual identification of the particles or features being tracked. This procedure, while thought to be reasonably accurate, is cumbersome and also certainly not as sophisticated as state of the art fully computerized Particle Image Velocimetry (PIV) or Particle Tracking Velocimetry (PTV).

Figure D.1: Sand Velocity Measurement End View

Figure D.2: Sand Velocity Measurement End View, with Dark Sand

Figure D.3: Sand Velocity Measurement Normal View

Figure D.4: Sand Velocity Measurement Normal View, with Dark Sand

APPENDIX E

WATTMETER SYSTEM SETUP

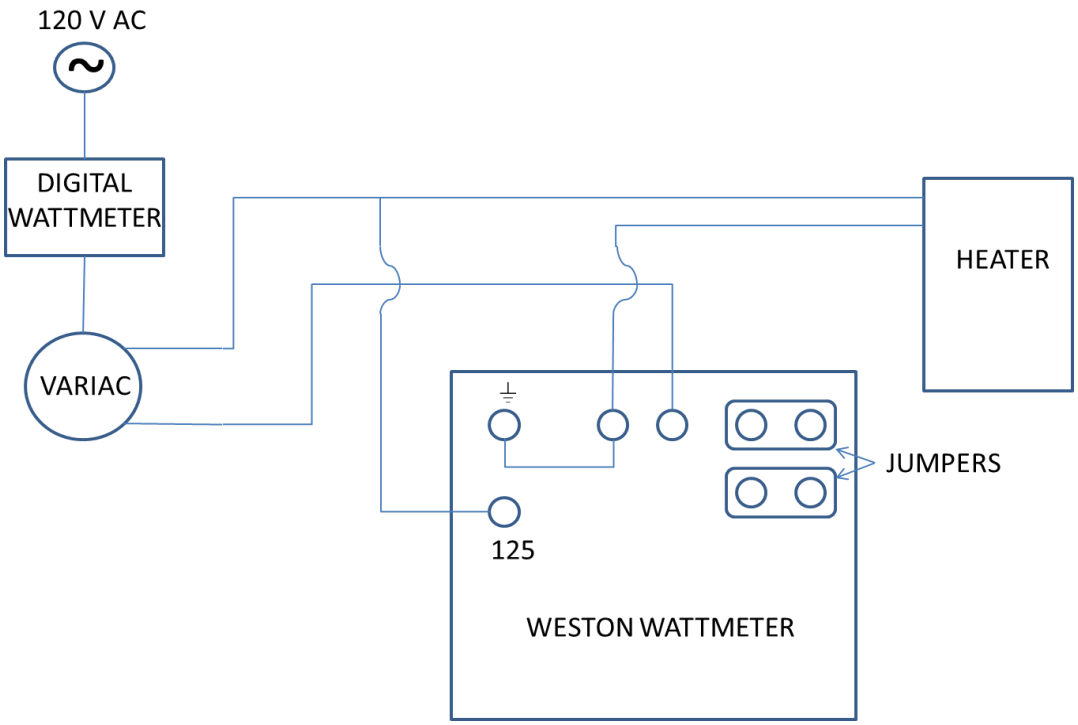

onnection Diagrams

tions for Measuring D. C. and Single Phase A. C. Power

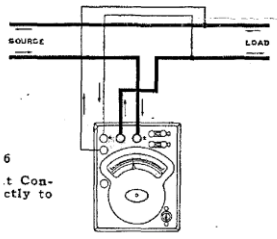

6
t Con-
ctly to

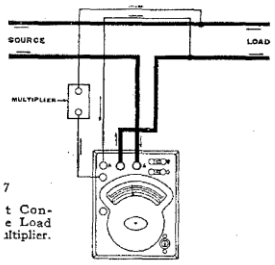

7
t Con-
e Load
ltiplier.

Connections for Measuring Single Phase A. C. Power

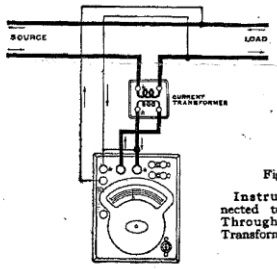

Figure 8
Instrument Connected to the Load Through a Current Transformer.

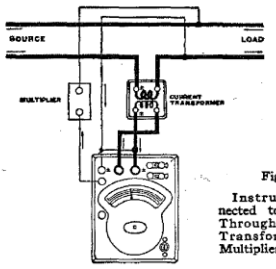

Figure 9
Instrument Connected to the Load Through a Current Transformer and a Multiplier.

See Caution Note on page 21.

Figure E.1: Wattmeter System Diagram

APPENDIX F

THERMOCOUPLE TO 4 WIRE RTD CALIBRATION

This appendix regards the calibration of thermocouples utilized in the rotating drum heat transfer experiment. Calibrations were done with a standardized 4 Wire RTD in a thermocouple calibrator (thermally insulated, internally heated and regulated box).

Table F.1: Thermocouple, 4 Wire RTD Measurements for Calibration

TC calibration 2010 field calibration, 26 Oct 04, updated 23 May 2005

est bias
0.02 C

avg

	y	x						
RTD 4W Resist	RTD Temp	TC 02	TC 03	TC 04	TC 05	TC 06	TC Average	RTD-TCave
Ohms	Celcius	oC	oC	oC	oC	oC	oC	oC
112.41	31.2494	31.42	31.38	31.38	31.38	31.42	31.40	-0.15
116.17	40.7837	40.26	40.07	40.43	40.16	40.39	40.26	0.52
120.51	51.8234	51.36	51.23	51.37	51.29	51.49	51.35	0.48
124.43	61.8271	61.09	60.91	61.09	61.95	61.25	61.26	0.57
128.26	71.6309	70.49	70.26	70.52	70.35	70.78	70.48	1.15
132.22	81.7986	80.17	79.91	80.28	80.06	80.58	80.20	1.60
136.11	91.8178	89.91	89.62	90.04	89.82	90.36	89.95	1.87
140.10	102.1268	99.84	99.51	99.96	99.74	100.39	99.89	2.24
143.86	111.8718	109.19	108.82	109.34	109.08	109.81	109.25	2.62
147.81	122.1409	119.19	118.81	119.38	119.08	119.86	119.26	2.88
151.62	132.0771	128.78	128.34	128.96	128.66	129.52	128.85	3.23
155.69	142.7254	138.91	138.43	139.19	138.81	139.81	139.03	3.70
159.45	152.5940	148.60	148.08	148.84	148.44	149.50	148.69	3.90
163.27	162.6513	158.28	157.74	158.55	158.16	159.29	158.40	4.25
167.03	172.5814	167.85	167.26	168.13	167.74	168.94	167.98	4.60
163.08	162.1503	157.87	157.31	158.09	157.67	158.79	157.95	4.20
159.26	152.0946	148.52	148.08	148.58	148.34	149.32	148.57	3.53
155.42	142.0179	138.48	138.04	138.66	138.36	139.3	138.568	3.45
151.71	132.3122	129.42	129.04	129.48	129.22	130.04	129.44	2.87
147.68	121.8024	119.22	118.88	119.27	119.06	119.8	119.246	2.56
143.79	111.6901	109.78	109.55	109.69	109.61	110.23	109.772	1.92
140.11	102.1527	100.28	100.02	100.26	100.12	100.7	100.28	1.88
136.20	92.0500	90.82	90.66	90.67	90.68	91.14	90.79	1.26
132.16	81.6443	80.39	80.17	80.38	80.24	80.69	80.37	1.27
128.30	71.7334	72.13	72.19	71.61	71.87	72.01	71.96	-0.23
124.36	61.6482	61.03	60.86	61.00	60.88	61.17	60.99	0.66
120.37	51.4667	50.95	50.79	50.95	50.81	51.09	50.92	0.55
116.35	41.2408	41.29	41.15	41.22	41.13	41.29	41.22	0.02
112.33	31.0469	31.41	31.32	31.34	31.27	31.32	31.332	-0.29
AVG =	99.47	97.48	97.19	97.54	97.38	97.94	97.51	1.97

Table F.2: Thermocouple 2 Calibration

Results for	**TC02**		
a	constant =	-1.5338	-1.53
b	coefficient =	1.0362	1.04
	U_A =	0.20	
	U_C =	0.20	

RTD 4W Resist Ohms	RTD Temp Celcius	RAW	CORR TC 02 oC	RAW-COR TC	RTD-TC	abs(DT)
112.41	31.2494	31.42	31.02	0.40	0.23	0.23
116.17	40.7837	40.26	40.18	0.08	0.60	0.60
120.51	51.8234	51.36	51.69	-0.32	0.14	0.14
124.43	61.8271	61.09	61.77	-0.68	0.06	0.06
128.26	71.6309	70.49	71.51	-1.02	0.12	0.12
132.22	81.7986	80.17	81.54	-1.37	0.26	0.26
136.11	91.8178	89.91	91.63	-1.72	0.19	0.19
140.10	102.1268	99.84	101.92	-2.08	0.21	0.21
143.86	111.8718	109.19	111.61	-2.42	0.26	0.26
147.81	122.1409	119.19	121.97	-2.78	0.17	0.17
151.62	132.0771	128.78	131.91	-3.13	0.17	0.17
155.69	142.7254	138.91	142.40	-3.49	0.32	0.32
159.45	152.5940	148.60	152.44	-3.84	0.15	0.15
163.27	162.6513	158.28	162.47	-4.19	0.18	0.18
167.03	172.5814	167.85	172.39	-4.54	0.19	0.19
163.08	162.1503	157.87	162.05	-4.18	0.10	0.10
159.26	152.0946	148.52	152.36	-3.84	-0.27	0.27
155.42	142.0179	138.48	141.96	-3.48	0.06	0.06
151.71	132.3122	129.42	132.57	-3.15	-0.26	0.26
147.68	121.8024	119.22	122.00	-2.78	-0.20	0.20
143.79	111.6901	109.78	112.22	-2.44	-0.53	0.53
140.11	102.1527	100.28	102.37	-2.09	-0.22	0.22
136.20	92.0500	90.82	92.57	-1.75	-0.52	0.52
132.16	81.6443	80.39	81.77	-1.38	-0.12	0.12
128.30	71.7334	72.13	73.21	-1.08	-1.47	1.47
124.36	61.6482	61.03	61.70	-0.67	-0.06	0.06
120.37	51.4667	50.95	51.26	-0.31	0.21	0.21
116.35	41.2408	41.29	41.25	0.04	-0.01	0.01
112.33	31.0469	31.41	31.01	0.40	0.03	0.03
AVG =	99.47	97.48	99.47	-1.99	0.00	0.25

Table F.3: Thermocouple 3 Calibration

Results for	**TC03**	
a	constant =	-1.5950
b	coefficient =	1.0399
	U_A =	0.24
	U_C =	0.24

RTD 4W Resist Ohms	RTD Temp Celcius	RAW	CORR TC 02 oC	RAW-CORR TC	RTD-TC	abs(DT)
112.41	31.2494	31.38	31.04	0.34	0.21	0.21
116.17	40.7837	40.07	40.08	-0.01	0.71	0.71
120.51	51.8234	51.23	51.68	-0.45	0.14	0.14
124.43	61.8271	60.91	61.75	-0.84	0.08	0.08
128.26	71.6309	70.26	71.47	-1.21	0.16	0.16
132.22	81.7986	79.91	81.51	-1.60	0.29	0.29
136.11	91.8178	89.62	91.60	-1.98	0.21	0.21
140.10	102.1268	99.51	101.89	-2.38	0.24	0.24
143.86	111.8718	108.82	111.57	-2.75	0.30	0.30
147.81	122.1409	118.81	121.96	-3.15	0.18	0.18
151.62	132.0771	128.34	131.87	-3.53	0.21	0.21
155.69	142.7254	138.43	142.36	-3.93	0.36	0.36
159.45	152.5940	148.08	152.40	-4.32	0.19	0.19
163.27	162.6513	157.74	162.45	-4.71	0.21	0.21
167.03	172.5814	167.26	172.35	-5.09	0.24	0.24
163.08	162.1503	157.31	162.00	-4.69	0.15	0.15
159.26	152.0946	148.08	152.40	-4.32	-0.31	0.31
155.42	142.0179	138.04	141.96	-3.92	0.06	0.06
151.71	132.3122	129.04	132.60	-3.56	-0.29	0.29
147.68	121.8024	118.88	122.03	-3.15	-0.23	0.23
143.79	111.6901	109.55	112.33	-2.78	-0.64	0.64
140.11	102.1527	100.02	102.42	-2.40	-0.27	0.27
136.20	92.0500	90.66	92.69	-2.03	-0.64	0.64
132.16	81.6443	80.17	81.78	-1.61	-0.13	0.13
128.30	71.7334	72.19	73.48	-1.29	-1.75	1.75
124.36	61.6482	60.86	61.70	-0.84	-0.05	0.05
120.37	51.4667	50.79	51.22	-0.43	0.24	0.24
116.35	41.2408	41.15	41.20	-0.05	0.04	0.04
112.33	31.0469	31.32	30.98	0.34	0.07	0.07
AVG =	99.47	97.19	99.47	-2.29	0.00	0.30

Table F.4: Thermocouple 4 Calibration

Results for	**TC04**	
a	constant =	-1.3661
b	coefficient =	1.0338
	U_A =	0.13
	U_C =	0.13

RTD 4W Resist Ohms	RTD Temp Celcius	RAW	CORR TC 02 oC	RAW-CORR TC	RTD-TC	abs(DT)
112.41	31.2494	31.38	31.08	0.30	0.17	0.17
116.17	40.7837	40.43	40.43	0.00	0.35	0.35
120.51	51.8234	51.37	51.74	-0.37	0.09	0.09
124.43	61.8271	61.09	61.79	-0.70	0.04	0.04
128.26	71.6309	70.52	71.54	-1.02	0.09	0.09
132.22	81.7986	80.28	81.63	-1.35	0.17	0.17
136.11	91.8178	90.04	91.72	-1.68	0.10	0.10
140.10	102.1268	99.96	101.98	-2.02	0.15	0.15
143.86	111.8718	109.34	111.67	-2.33	0.20	0.20
147.81	122.1409	119.38	122.05	-2.67	0.09	0.09
151.62	132.0771	128.96	131.96	-3.00	0.12	0.12
155.69	142.7254	139.19	142.53	-3.34	0.19	0.19
159.45	152.5940	148.84	152.51	-3.67	0.08	0.08
163.27	162.6513	158.55	162.55	-4.00	0.10	0.10
167.03	172.5814	168.13	172.45	-4.32	0.13	0.13
163.08	162.1503	158.09	162.07	-3.98	0.08	0.08
159.26	152.0946	148.58	152.24	-3.66	-0.15	0.15
155.42	142.0179	138.66	141.99	-3.33	0.03	0.03
151.71	132.3122	129.48	132.50	-3.02	-0.18	0.18
147.68	121.8024	119.27	121.94	-2.67	-0.14	0.14
143.79	111.6901	109.69	112.04	-2.35	-0.35	0.35
140.11	102.1527	100.26	102.29	-2.03	-0.13	0.13
136.20	92.0500	90.67	92.37	-1.70	-0.32	0.32
132.16	81.6443	80.38	81.73	-1.35	-0.09	0.09
128.30	71.7334	71.61	72.67	-1.06	-0.93	0.93
124.36	61.6482	61.00	61.70	-0.70	-0.05	0.05
120.37	51.4667	50.95	51.31	-0.36	0.16	0.16
116.35	41.2408	41.22	41.25	-0.03	-0.01	0.01
112.33	31.0469	31.34	31.03	0.31	0.01	0.01
AVG =	99.47	97.54	99.47	-1.93	0.00	0.16

Table F.5: Thermocouple 5 Calibration

Results for	**TC05**					
a	constant =	-1.5238				
b	coefficient =	1.0372				
	U_A =	0.21				
	U_C =	0.21				
		RAW	CORR	RAW-CORR		
RTD 4W Resist	RTD Temp		TC 02	TC	RTD-TC	abs(DT)
Ohms	Celcius		oC			
112.41	31.2494	31.38	31.02	0.36	0.23	0.23
116.17	40.7837	40.16	40.13	0.03	0.65	0.65
120.51	51.8234	51.29	51.67	-0.38	0.15	0.15
124.43	61.8271	61.95	62.73	-0.78	-0.90	0.90
128.26	71.6309	70.35	71.44	-1.09	0.19	0.19
132.22	81.7986	80.06	81.51	-1.45	0.29	0.29
136.11	91.8178	89.82	91.63	-1.81	0.18	0.18
140.10	102.1268	99.74	101.92	-2.18	0.20	0.20
143.86	111.8718	109.08	111.61	-2.53	0.26	0.26
147.81	122.1409	119.08	121.98	-2.90	0.16	0.16
151.62	132.0771	128.66	131.92	-3.26	0.16	0.16
155.69	142.7254	138.81	142.45	-3.64	0.28	0.28
159.45	152.5940	148.44	152.43	-3.99	0.16	0.16
163.27	162.6513	158.16	162.51	-4.35	0.14	0.14
167.03	172.5814	167.74	172.45	-4.71	0.13	0.13
163.08	162.1503	157.67	162.01	-4.34	0.14	0.14
159.26	152.0946	148.34	152.33	-3.99	-0.24	0.24
155.42	142.0179	138.36	141.98	-3.62	0.04	0.04
151.71	132.3122	129.22	132.50	-3.28	-0.19	0.19
147.68	121.8024	119.06	121.96	-2.90	-0.16	0.16
143.79	111.6901	109.61	112.16	-2.55	-0.47	0.47
140.11	102.1527	100.12	102.32	-2.20	-0.16	0.16
136.20	92.0500	90.68	92.53	-1.85	-0.48	0.48
132.16	81.6443	80.24	81.70	-1.46	-0.05	0.05
128.30	71.7334	71.87	73.02	-1.15	-1.28	1.28
124.36	61.6482	60.88	61.62	-0.74	0.03	0.03
120.37	51.4667	50.81	51.17	-0.36	0.29	0.29
116.35	41.2408	41.13	41.13	0.00	0.11	0.11
112.33	31.0469	31.27	30.91	0.36	0.14	0.14
AVG =	99.47	97.38	99.47	-2.10	0.00	0.27

Table F.6: Thermocouple 6 Calibration

Results for	**TC06**	
a	constant =	-1.2016
b	coefficient =	1.0279
	U_A =	0.15
	U_C =	0.15

RTD 4W Resist Ohms	RTD Temp Celcius	RAW	CORR TC 02 oC	RAW-CORR TC	RTD-TC	abs(DT)
112.41	31.2494	31.42	31.10	0.32	0.15	0.15
116.17	40.7837	40.39	40.32	0.07	0.47	0.47
120.51	51.8234	51.49	51.73	-0.24	0.09	0.09
124.43	61.8271	61.25	61.76	-0.51	0.06	0.06
128.26	71.6309	70.78	71.55	-0.77	0.08	0.08
132.22	81.7986	80.58	81.63	-1.05	0.17	0.17
136.11	91.8178	90.36	91.68	-1.32	0.14	0.14
140.10	102.1268	100.39	101.99	-1.60	0.14	0.14
143.86	111.8718	109.81	111.67	-1.86	0.20	0.20
147.81	122.1409	119.86	122.01	-2.15	0.14	0.14
151.62	132.0771	129.52	131.93	-2.41	0.14	0.14
155.69	142.7254	139.81	142.51	-2.70	0.21	0.21
159.45	152.5940	149.50	152.47	-2.97	0.12	0.12
163.27	162.6513	159.29	162.54	-3.25	0.12	0.12
167.03	172.5814	168.94	172.46	-3.52	0.13	0.13
163.08	162.1503	158.79	162.02	-3.23	0.13	0.13
159.26	152.0946	149.32	152.29	-2.97	-0.19	0.19
155.42	142.0179	139.30	141.99	-2.69	0.03	0.03
151.71	132.3122	130.04	132.47	-2.43	-0.16	0.16
147.68	121.8024	119.80	121.94	-2.14	-0.14	0.14
143.79	111.6901	110.23	112.11	-1.88	-0.42	0.42
140.11	102.1527	100.70	102.31	-1.61	-0.16	0.16
136.20	92.0500	91.14	92.48	-1.34	-0.43	0.43
132.16	81.6443	80.69	81.74	-1.05	-0.10	0.10
128.30	71.7334	72.01	72.82	-0.81	-1.09	1.09
124.36	61.6482	61.17	61.68	-0.51	-0.03	0.03
120.37	51.4667	51.09	51.31	-0.22	0.15	0.15
116.35	41.2408	41.29	41.24	0.05	0.00	0.00
112.33	31.0469	31.32	30.99	0.33	0.05	0.05
AVG =	99.47	97.94	99.47	-1.53	0.00	0.19

Table F.7: Polynomial Regression Data, Calibration with 4 Wire RTD

Output from Poly_regress user form, S. M. Jeter, 24 Dec 03-2 Apr 04.
Note this sheet is mostly values with few active formulas. See notes at Cell B12

	Points =	29		R_sq =	0.999958		D of F =	27
	Vars =	1		SEE =	0.285013		k_c_raw =	2.051829
	Coef	U of Coef	Alpha R	Cond Coef	Cond U	X min	X max	X avg
Var 1	1.027922	0.001286	1.36E-60	1.027922	0.001286	31.32	168.94	97.94097

scaling not selected

k_c mult =	1	U_A avg =	0.149238
k_c plot =	2.051829	U_C avg =	0.150636

Notes to Users:
The coverage factor inflator in Cell M2 can be updated
The U_B uncertainty data in Column AF can be updated
Important average uncertainty data are in Cells O2 and O3
Average uncertainties above valid only if the M2 inflator is 1

	Y_raw	Y_corr	Y_model	X_block
Point 1	31.24943	31.24943	31.09576	31.42
Point 2	40.78368	40.78368	40.31622	40.39
Point 3	51.82342	51.82342	51.73027	51.494
Point 4	61.82708	61.82708	61.76279	61.254
Point 5	71.63087	71.63087	71.55478	70.78
Point 6	81.79864	81.79864	81.62842	80.58
Point 7	91.81781	91.81781	91.6815	90.36
Point 8	102.1268	102.1268	101.9916	100.39
Point 9	111.8718	111.8718	111.6746	109.81
Point 10	122.1409	122.1409	122.0052	119.86
Point 11	132.0771	132.0771	131.9349	129.52
Point 12	142.7254	142.7254	142.5123	139.81
Point 13	152.594	152.594	152.4728	149.5
Point 14	162.6513	162.6513	162.5362	159.29
Point 15	172.5814	172.5814	172.4556	168.94
Point 16	162.1503	162.1503	162.0222	158.79
Point 17	152.0946	152.0946	152.2878	149.32
Point 18	142.0179	142.0179	141.988	139.3
Point 19	132.3122	132.3122	132.4695	130.04
Point 20	121.8024	121.8024	121.9435	119.8
Point 21	111.6901	111.6901	112.1063	110.23
Point 22	102.1527	102.1527	102.3102	100.7
Point 23	92.04998	92.04998	92.48328	91.14
Point 24	81.64434	81.64434	81.74149	80.69
Point 25	71.73341	71.73341	71.73341	72.01
Point 26	61.64817	61.64817	61.64817	61.17
Point 27	51.46672	51.46672	51.31499	51.09
Point 28	41.24081	41.24081	41.24135	41.29
Point 29	31.04688	31.04688	30.99296	31.32

Table F.8: Regression Statistics, Calibration with 4 Wire RTD

SUMMARY OUTPUT

Regression Statistics	
Multiple R	0.9999789
R Square	0.9999577
Adjusted R Square	0.9999562
Standard Error	0.2850132
Observations	29

ANOVA

	df	*SS*	*MS*	*F*	*Significance F*
Regression	1	51889.038	51889.04	638771.6	1.35908E-60
Residual	27	2.193278674	0.081233		
Total	28	51891.23128			

	Coefficients	*Standard Error*	*t Stat*	*P-value*	*Lower 95%*	*Upper 95%*
Intercept	-1.2015644	0.13663254	-8.794131	2.07E-09	-1.481911017	-0.921218
X Variable 1	1.0279224	0.001286138	799.2319	1.36E-60	1.025283422	1.030561

APPENDIX G

HEAT TRANSFER COEFFICIENT REGRESSION ANALYSIS

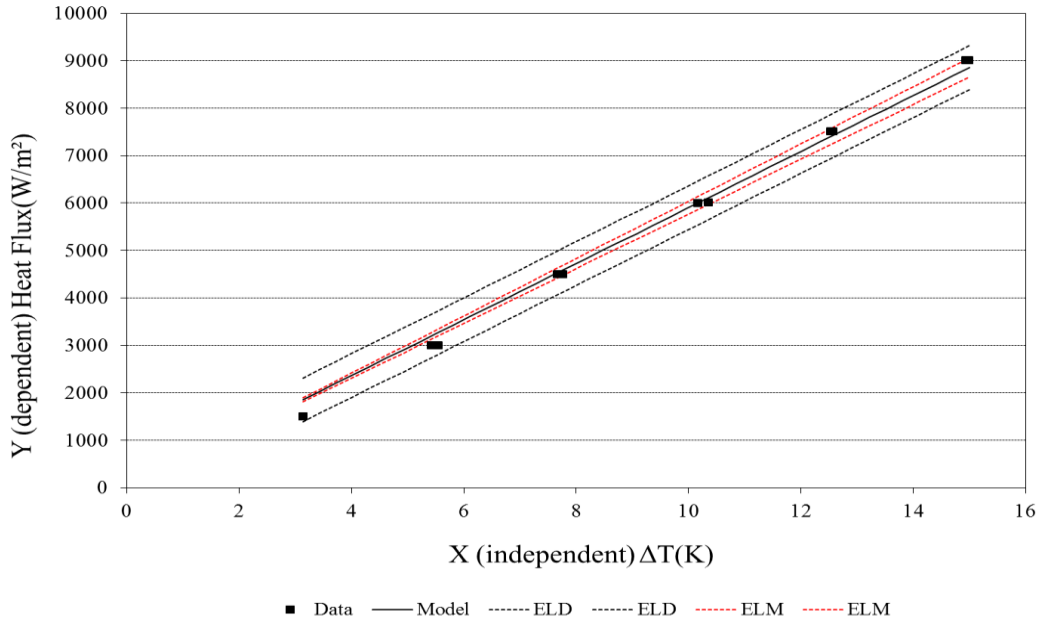

Figure G.1: Olivine Heat Transfer Coefficient Polynomial Regression

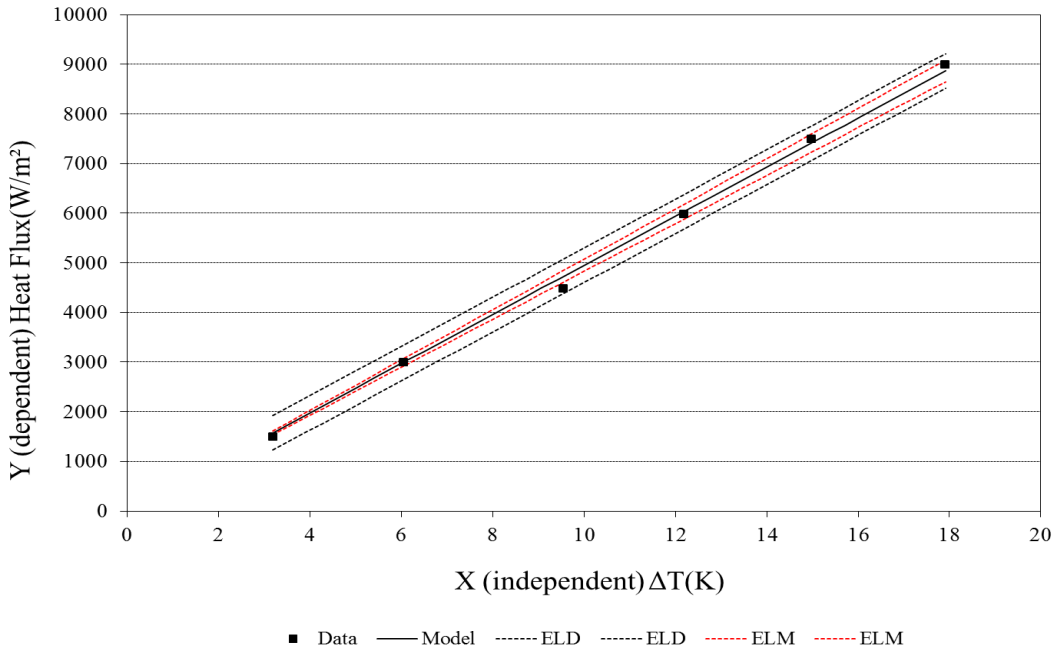

Figure G.2: Fine Sifted Silica Heat Transfer Coefficient Polynomial Regression

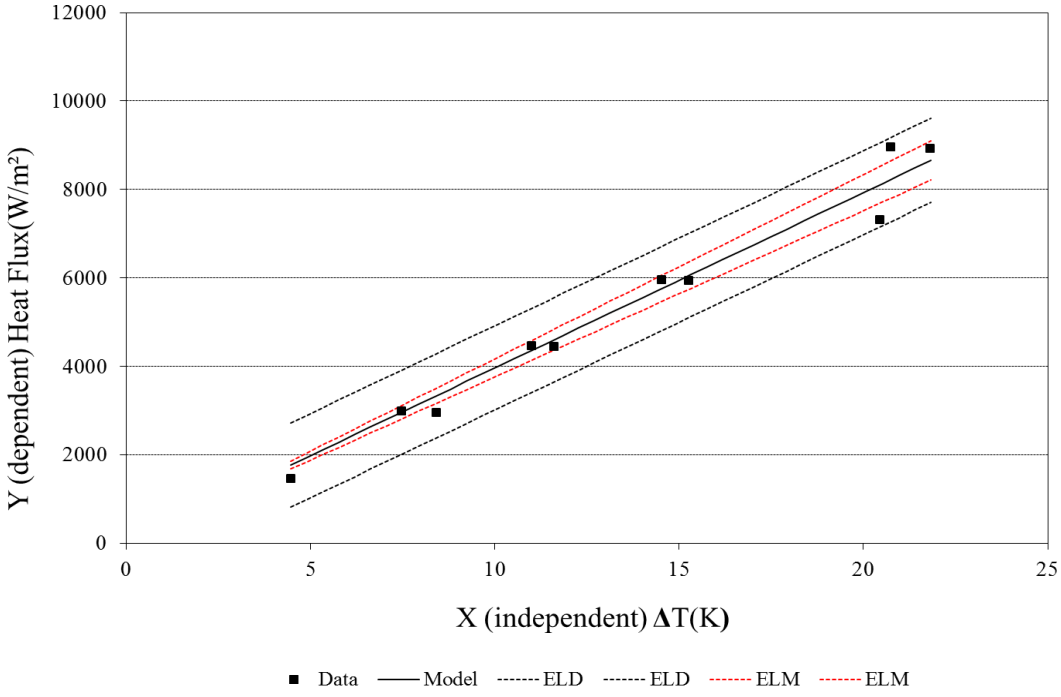

Figure G.3: Fine Silica Heat Transfer Coefficient Polynomial Regression

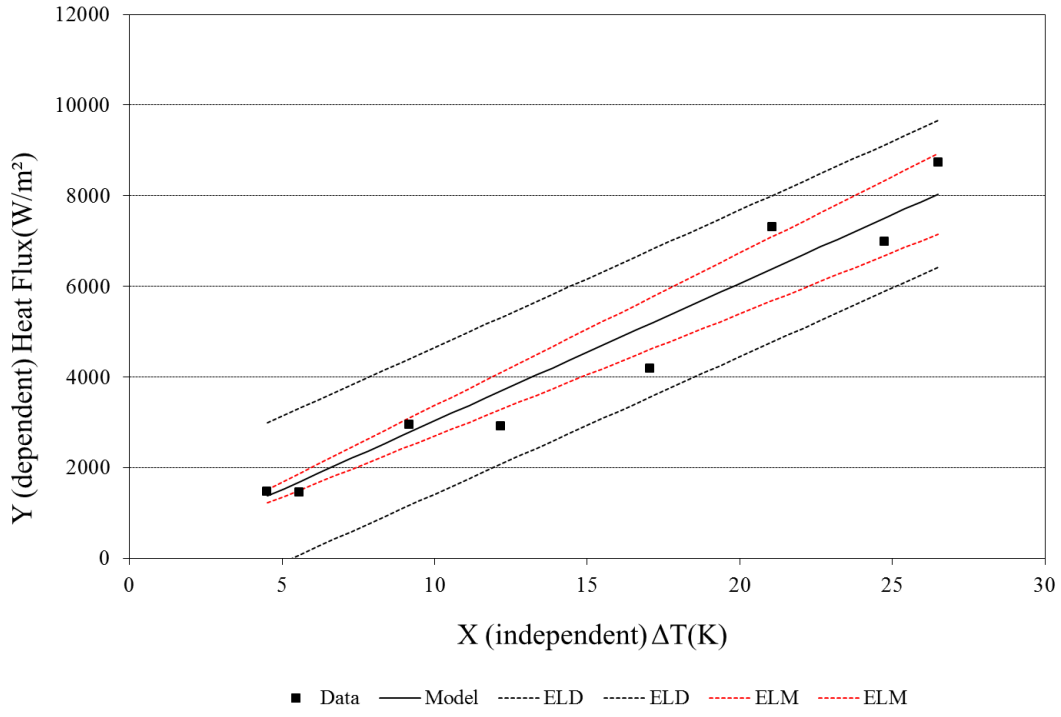

Figure G.4: Construction Silica Heat Transfer Coefficient Polynomial Regression

Table G.1: Olivine Heat Transfer Coefficient Regression Statistics

SUMMARY OUTPUT						
Regression Statistics						
Multiple R	0.99940947					
R Square	0.99881928					
Adjusted R Square	0.90791019					
Standard Error	209.703056					
Observations	12					
ANOVA						
	df	*SS*	*MS*	*F*	*Significance F*	
Regression	1	409206116.4	4.09E+08	9305.347	3.50994E-16	
Residual	11	483729.0905	43975.37			
Total	12	409689845.5				
	Coefficients	*Standard Error*	*t Stat*	*P-value*	*Lower 95%*	*Upper 95%*
Intercept	0	#N/A	#N/A	#N/A	#N/A	#N/A
X Variable 1	590.401413	6.120418087	96.46423	1.86E-17	576.9304631	603.8724
				U_A	13.47094938	

Table G.2: Fine Sifted Silica Heat Transfer Coefficient Regression Statistics

SUMMARY OUTPUT						
Regression Statistics						
Multiple R	0.99977327					
R Square	0.9995466					
Adjusted R Square	0.7995466					
Standard Error	135.974758					
Observations	6					
ANOVA						
	df	*SS*	*MS*	*F*	*Significance F*	
Regression	1	203800618.8	2.04E+08	11022.72	4.93527E-08	
Residual	5	92445.67428	18489.13			
Total	6	203893064.4				
	Coefficients	*Standard Error*	*t Stat*	*P-value*	*Lower 95%*	*Upper 95%*
Intercept	0	#N/A	#N/A	#N/A	#N/A	#N/A
X Variable 1	494.934972	4.714153153	104.9892	1.49E-09	482.8168553	507.05309
				U_A	12.11811646	

Table G.3: Fine Silica Heat Transfer Coefficient Regression Statistics

SUMMARY OUTPUT						
Regression Statistics						
Multiple R	0.99767253					
R Square	0.99535048					
Adjusted R Square	0.88423937					
Standard Error	421.038478					
Observations	10					
ANOVA						
	df	*SS*	*MS*	*F*	*Significance F*	
Regression	1	341549862.9	3.42E+08	1926.684	8.00751E-11	
Residual	9	1595460.599	177273.4			
Total	10	343145323.5				
	Coefficients	*Standard Error*	*t Stat*	*P-value*	*Lower 95%*	*Upper 95%*
Intercept	0	#N/A	#N/A	#N/A	#N/A	#N/A
X Variable 1	396.559099	9.034469352	43.89401	8.26E-12	376.1217099	416.99649
				U_A	20.43738952	

Table G.4: Construction Silica Heat Transfer Coefficient Regression Statistics

SUMMARY OUTPUT						
Regression Statistics						
Multiple R	0.99244865					
R Square	0.98495432					
Adjusted R Square	0.84209718					
Standard Error	684.154764					
Observations	8					
ANOVA						
	df	*SS*	*MS*	*F*	*Significance F*	
Regression	1	214492001.3	2.14E+08	458.2499	6.77898E-07	
Residual	7	3276474.187	468067.7			
Total	8	217768475.5				
	Coefficients	*Standard Error*	*t Stat*	*P-value*	*Lower 95%*	*Upper 95%*
Intercept	0	#N/A	#N/A	#N/A	#N/A	#N/A
X Variable 1	303.286456	14.16778055	21.40677	1.22E-07	269.7849788	336.7879
				U_A	33.50147748	

APPENDIX H

HEAT TRANSFER COEFFICIENT DATA, THIN FILM TC

Table H.1: Thin Film Thermocouple Heat Transfer Coefficient Data

Olivine					
ΔT_Air(°K)	ΔT_Sand(°K)	Power_Air(W)	Power_Sand(W)	Heat_Flux_Sand(W/K-m²)	h_Sand(W/K-m²)
6.789664	3.13725	0.870608401	19.1293916	1491.854907	475.5295
12.4805955	5.423446	1.600331222	38.39966878	2994.697139	552.1761
18.031493	7.6775575	2.312098107	57.68790189	4498.939712	585.9858
23.993944	10.169154	3.076636666	76.92336333	5999.066749	589.9278
29.3744545	12.5384325	3.766555584	96.23344442	7505.013191	598.5607
35.3549085	14.9469475	4.533402588	115.4665974	9004.960198	602.4615
6.9202435	3.148321	0.887352029	19.11264797	1490.549112	473.4425
12.4664735	5.553757	1.598520421	38.40147958	2994.838359	539.2455
18.2044235	7.769333	2.334272216	57.66572778	4497.210407	578.8412
23.9391765	10.3608395	3.069614073	76.93038593	5999.614424	579.0664
29.480247	12.5749895	3.780120886	96.21987911	7503.955266	596.7365
35.1190085	15.003721	4.50315418	115.4968458	9007.319198	600.339

Fine Sifted Silica					
ΔT_Air(°K)	ΔT_Sand(°K)	Power_Air(W)	Power_Sand(W)	Heat_Flux_Sand(W/K-m²)	h_Sand(W/K-m²)
6.7378195	3.1865385	0.863960611	19.13603939	1492.373352	468.3368
13.02665	6.0459165	1.670349361	38.32965064	2989.236594	494.4224
20.118594	9.5555855	2.579717781	57.42028222	4478.068702	468.6336
25.555522	12.1829835	3.276870864	76.72312914	5983.450969	491.1318
31.0032245	14.985482	3.975405513	96.02459449	7488.725491	499.732
36.9930055	17.915548	4.743448476	115.2565515	8988.579228	501.7195

Fine Silica					
ΔT_Air(°K)	ΔT_Sand(°K)	Power_Air(W)	Power_Sand(W)	Heat_Flux_Sand(W/K-m²)	h_Sand(W/K-m²)
9.7326315	4.4580375	1.247972027	18.75202797	1462.425232	328.0424
14.4097505	7.4767765	1.847698183	38.15230182	2975.405589	397.953
17.472094	8.4245905	2.240368863	37.75963114	2944.782154	349.546
21.339179	10.9918495	2.736227964	57.26377204	4465.862852	406.2886
23.5584365	11.6169235	3.020793477	56.97920652	4443.670277	382.517
28.132608	14.533007	3.607319134	76.39268087	5957.680109	409.9413
30.6000415	15.2577485	3.923707151	76.07629285	5933.005774	388.852
49.5848245	20.45594	6.358041393	93.64195861	7302.909491	357.0068
40.080141	20.7490565	5.139298124	114.8607019	8957.707873	431.7164
44.087552	21.826419	5.653150603	114.3468494	8917.633763	408.5706

Construction Silica					
ΔT_Air(°K)	ΔT_Sand(°K)	Power_Air(W)	Power_Sand(W)	Heat_Flux_Sand(W/K-m²)	h_Sand(W/K-m²)
8.841853	4.517427	1.133751464	18.86624854	1471.333017	325.7016
10.1202935	5.572811	1.2976802	18.7023198	1458.548612	261.7258
17.404024	9.174893	2.23164055	37.76835945	2945.462854	321.0351
21.091492	12.1773675	2.704468162	37.29553184	2908.588174	238.852
48.95939	17.0490875	6.27784471	53.72215529	4189.660742	245.7411
80.339305	24.7335015	10.30155157	89.69844843	6995.364686	282.8295
48.6259455	21.058859	6.235088606	93.76491139	7312.498281	347.241
61.896475	26.4962375	7.93670955	112.0632905	8739.544533	329.841

REFERENCES

[1] Süle, Z., Mihálykó, C., Lakatos, B., **"**Modeling of heat transfer processes in particulate systems", *16th European Symposium on Computer Aided Process Engineering and 9th International Symposium on Process Systems Engineering*, 2006

[2] Sun, J., Chen, M.M., "A theoretical analysis of heat transfer due to particle impact" *Int. J. Hear Mass Transfer*. Vol. 31, No. 5, 1988, Pages 969-975

[3] Natale, F., Lancia, A., Nigro, R., "Surface-to-bed heat transfer in fluidised beds of fine particles", *Powder Technology,* Vol. 195, 2009, Pages 135–142

[4] Vargas, W., McCarthy, J.J., "Heat Conduction in Granular Materials", *AIChE Journal,* Vol. 47, No. 5, May 2001, Pages 1052-1059

[5] Vargas, W., McCarthy, J.J., "Conductivity of granular media with stagnant interstitial fluids via thermal particle dynamics simulation", *International Journal of Heat and Mass Transfer*, Issue 45, 2002, Pages 4847–4856

[6] Vargas-Escobar, W., "Discrete Modeling of Heat Conduction in Granular Media", *University of Pittsburgh Thesis*, 2002

[7] Lun, C.K.K., Savage, S.B., Jeffery, D. J., Chepurniy, N., "Kinetic theories for granular flow: inelastic particles in Couette flow and slightly inelastic particles in a general flowfield", *J. Fluid Mech.*, vol. 140, 1984, Pages 223-256

[8] Thompson, P., Grest, G., "Granular Flow: Friction and the Dilatancy Transition", *Physical Review Letters*, Vol. 67, No. 13, Sep. 1991, Pages 1751-1754

[9] Baxter, G.W., Leone, R., Behringe, R.P., "Experimental Test of Time Scales in Flowing Sand", *Europhyics Letters,* Vol. 21, No 5, 1993, Pages 569-574

[10] Shi, D., Vargas, W., McCarthy, J.J., "Heat transfer in rotary kilns with interstitial gases", *Chemical Engineering Science,* Vol. 63, 2008, Pages 4506-4516

[11] Chaudhuri, B., Muzzio, F.J., Tomassone, M.S., "Modeling of heat transfer in granular flowing rotating vessels", *Chemical Engineering Science*, Volume 61, 2006, Pages 6348 – 6360

[12] Molerus, O., "Heat transfer in moving beds with a stagnant interstitial gas", *International Journal of Heat and Mass Transfer*, Vol. 40, No. 17, 1997, Pages 4151-4159

[13] Brinn, M.S., Friedman, S.J., Gluckert, F.A., Pigford, R.L., "Heat transfer to granular materials, settled beds moving downwards through vertical pipes", *Industrial and Engineering Chemistery*, Vol. 40, No. 6, June 1948, Pages 1250-1261

[14] Denloye, A.O.O., Botterill, J.S.M., "Heat transfer in flowing packed beds", *Chemical Engineering Science*, Volume 32. 1977, Pages 461-465

[15] Hyde, M., Klocke, H.-J., "Heat transfer between fluidized beds and heat exchange installations", *International Chemical Engineering*, Vol. 20, No. 4., 1980, Pages 583-599

[16] Patton, J.S., Sabersky, R.H., Brennen, C.E., "Convective heat transfer to rapidly flowing, granular materials", *International Journal of Heat and Mass Transfer*, Vol. 29, No. 8, August 1986, Pages 1263-1269

[17] Babcock and Wilcox, "Selection and Conceptual Design of an Advanced Thermal Energy Storage Subsystem for Commercial Scale (100 MWe) Solar Central Receiver Power Plant", Nuclear Power Group, Nuclear Power Generation Division, 1981, Lynchburg, Virginia

[18] Green, H.J., Cécile, M.L., Bohn, M.S., "Technical and Economic Evaluation of a Solid-Particle/Air Direct-Contact Heat Exchanger", Solar Energy Research Institute, Division of Midwest Research Institute, 1986, Golden, Colorado

[19] Klein, S.A., "Engineering Equation Solver", F-Chart Software, 2010, www.fChart.com

[20] Muchowski, E., "Heat transfer from the bottoms of vibrated vessels to packings of spheres at atmospheric pressure and under vacuum", *International Chemical Engineering*, Vol. 20, No. 4., 1980, Pages 564-582

[21] Wunschmann, J., Schlünder, E.U., "Heat transfer from heated surfaces to spherical packings", *International Chemical Engineering*, Vol. 20, No. 4., 1980, Pages 555-563

[22] "Cromgard, CR-12 Steel", American Utility Metals, 2010, Baton Rouge, Louisiana, www.cromgard.com

[23] "Logger Pro 3", Vernier Software & Technology, 2011, www.vernier.com

[24] Kreith F., Black, W.Z., "Basic Heat Transfer", Harper and Row, 1980, New York

[25] McAdams, W.H., "Heat Transmission", 3rd ed., McGraw-Hill Book Company, Inc., 1954, New York

[26] "Platinum Resistance Thermometer", Burns Engineering, 2004, Minnetonka, MN

[27] "DB-700A Block Calibrator", Techne Laboratory Equipment, 2011, Cambridge, U.K.

[28] "LE 280", Piedmont Foundry Supply, Inc., 2010, Oakboro, North Carolina, www.piedmontfoundrysupply.com

[29] "Granusil 7005/4010", Unimin Corporation, 2010, New Canaan, Connecticut, www.unimin.com

[30] "Carbo HSP™ High Strength Ceramic Proppant 20/40", Carbo Ceramics, 2010, Houston, Texas, www.carboceramics.com

[31] "Digital Camera EX-FH25", CASIO, 2011, www.casio-intl.com/dc/